DOKUZ EYLÜL UNIVERSITY

GRADUATE SCHOOL OF NATURAL AND APPLIED SCIENCES

COMPUTER ANALYSIS OF RETINAL IMAGES FOR VESSEL ANOMALY DETECTION

by

Shahab ASLANI

December, 2015

İZMİR

COMPUTER ANALYSIS OF RETINAL IMAGES FOR VESSEL ANOMALY DETECTION

A Thesis Submitted to the
Graduate School of Natural and Applied Sciences of Dokuz Eylül University
In Partial Fulfillment of the Requirements for the Degree of Master of Science
in Electrical and Electronics Engineering Program

by

Shahab ASLANI

December, 2015

İZMİR

M.SC THESIS EXAMINATION RESULT FORM

We have read the thesis entitled **"COMPUTER ANALYSIS OF RETINAL IMAGES FOR VESSEL ANOMALY DETECTION"** completed by **SHAHAB ASLANI** under supervision of **ASST. PROF. DR. HALDUN SARNEL** and we certify that in our opinion it is fully adequate, in scope and in quality, as a thesis for the degree of Master of Science

Asst. Prof. Dr. Haldun SARNEL

Supervisor

Asst Prof Dr. Yavuz Sönü

Jury Member

Assoc. Prof. Dr. Muhammed Cinsdikici

Jury Member

Prof. Dr. Ayşe OKUR
Director
Graduate School of Natural and Applied Sciences

ACKNOWLEDGMENTS

First of all, I would like to thank and express my sincere gratitude to my supervisor, Asst. Prof. Dr. Haldun Sarnel for his valuable support, educational moral and encouraging words throughout my study. I am greatly indebted to him for accepting me as his student and giving me an opportunity to work towards my M.Sc. degree under his patient guidance.

I am especially thankful to Dr. Nima Hatami who offered a valuable guidance in utilizing machine learning algorithms knowledge into a retinal image analysis, owing to his experience and expertise.

Living abroad far from family and hometown for the first time was a nice challenge. But you will learn to find new friends. Beyda was one who accepted me as a friend and helped me like kardeş. My special thank goes to my dear friends, my home mates and my brothers, Amir and Mohammad, who were there anytime I needed.

Finally, and most importantly, I would like to extend special thanks to my parents, Behzad and Homeyra for their sacrifices, inspiration and patients throughout my studies. Without their full support and love, this thesis would not have been possible to achieve. I am also thankful to my lovely sisters, Saba and Fereshte, who supported me, trusted me and loved me.

Shahab ASLANI

COMPUTER ANALYSIS OF RETINAL IMAGES FOR VESSEL ANOMALY DETECTION

ABSTRACT

Many important eye diseases, as well as systemic diseases such as diabetes, hypertension and arteriosclerosis manifest themselves in the retina. An automatic analysis of the vascular system of the retina can assist to monitor the effects of corresponding diseases on the visual system. In this thesis, we have presented a robust method for retinal blood vessel segmentation and some automatic algorithms for analyzing the vessel network with regard to the vessel diameter and tortuosity.

A supervised method is presented for segmentation of retinal blood vessels using an ensemble classifier of random forest decision trees. A 17 dimensional feature vector is constructed for successfully handling the both normal and abnormal retinal images with different kinds of lesions. Forty retina images from DRIVE database and twenty images from STARE database are used to evaluate the performance of the method. The results of performance metrics illustrate that the proposed method outperforms most of the other segmentation methods. Moreover, our method needs fewer samples for training than other methods and it is independent to the training set as it offers a better performance than other methods in the cross-training section.

The automatic method for measuring the retinal vessel width and tortuosity is also presented based on the vessel edges and centerline in order to analysis the vessel network and monitor the presence of different abnormalities in the structure of vessels. This application may assist to quick diagnosis and treatment planning in the clinical procedures.

Keywords: Retinal blood vessels segmentation, feature vector, ensemble classifier, vessel width and tortuosity measurement.

RETİNA GÖRÜNTÜLERİNİN DAMAR ANOMALİ BELİRLEMEK AMACIYLA BİLGİSAYARDA ANALİZİ

ÖZ

Birçok önemli göz hastalığının yanı sıra, diyabet, Hipertansiyon ve damar sertliği gibi sistemik hastalıklar da, retinada kendini göstermektedir. Retina vaskuler systemının otomatık analızı, yukardakı hastalıkların etıkısını gorsel sistemde, gostermeye yardımcı olmaktadır. Bu tezde, retina damar segmentasyonu için sağlam bir yöntem ve damar ağını analiz etmek için damar çapı ve kıvrımlarıyla ilgili otomatik bir algoritma sunulmustur.

Denetlenen yöntem, rasgele orman karar ağaçlarının bir topluluk sınıflandırıcı kullanarak, retina kan damarlarının segmentasyonu için sunulmuştur. 17 boyut özelik vektörü, normal ve farklı tür anormal retina lezyonlarinin görüntüleri Başarıyla inşa edilmiştir. DRIVE veri tabanindan alinan Kırk görüntü ve STARE veritabanından alinan yirmi görüntü retinanın yöntem performansını değerlendirmek için kullanilmistir. Performans ölçümlerinin sonuçları, önerilen yöntemin diğer segmentasyon yöntemlerinden daha iyi sonuçlar verdiğini gostermektedir. Ayrıca, bizim yöntem diğer yöntemlere göre, eğitim için daha az örnege ihtiyacı vardir ve bu very yonteminden bağımsızdır cunku çapraz eğitim bölümünde daha iyi bir performans sunmaktadir.

Retina damar genişliği ölçme ve eğrilik için otomatik yöntem sunulmaktadir. Damarı kenarı ve merkezini damar ağını analiz etmesi ve gemilerin yapısında farklı anormalliklerin varlığını izlemeye goredir. Bu uygulama, klinik hızlı teşhis ve tedavi planlamasına yardımcı olmaktadir.

Anahtar kelimeler: Retina kan damarları segmentasyonu, özellik vektörü, ensemble sınıflandırıcı, damar genişliği ve kıvrılma ölçümü.

CONTENTS

Page

LIST OF FIGURES

Page

LIST OF TABLES

Page

CHAPTER ONE
INTRODUCTION

1.1 Human Eye

One of the most important sensory system for amassing of information, learning and navigation is the human visual system. The eye is the initial sensor of the corresponding system with different lens mapping incoming light patterns on the retina for transduction to neural signals. There are many diseases that have primary and secondary effects on the retina and human visual system, so examination of the eye is a momentous part of health care.

1.1.1 Retinal Imaging

Fluorescein angiography is an early method for taking photographs of the fundus, or back of the eye, required the injection of fluorescein into blood stream to enhance the contrast of retinal blood vessels (Michaelson, & Benezra, 1980). However, with regarding advances in information and communication technology during last decade, digital fundus photography of retina has been developed (Klein et al., 2004). Fundus imaging is the process of obtaining the projection of the 3-D semitransparent retinal tissue onto the imaging plane as a 2-D representation using the reflected light and the image intensities to represent the amount of a reflected quantity of light (Abramoff, Garvin, & Sonka, 2010). There are several reasons why digital fundus images have been widely used in many projects. Firstly the publicity available databases have used fundus photographs of patients. Secondly this kind of photography is very useful for population-based and diagnose various type of systemic diseases such as diabetics, arteriosclerosis, and hypertension. Lastly and the most important advantage of corresponding images is possibility of precise measurement and monitoring of width and tortuosity of retinal blood vessels. Figure 1.1 illustrate an example of digital fundus image and a patient being examined with a digital fundus camera.

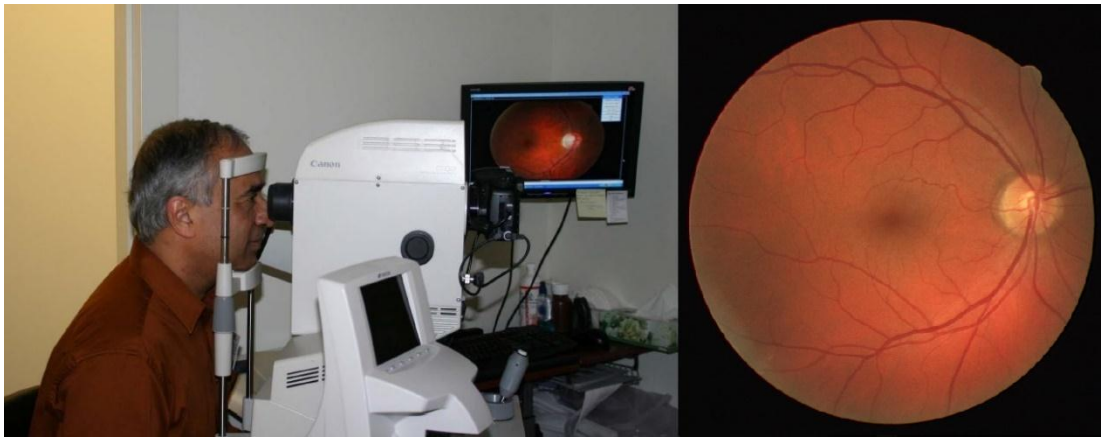

Figure 1.1 A general package of a digital fundus imaging includes a CR5-NM Canon retinal camera, a imaging software system, a database management system, a data store devise (Zhu, Rangayyan, & Ells, 2011).

1.1.2 Eye Anatomy

The eye is one of the most important sensors of the human body which gives us the sense of sight and allows us to see and comprehend the shapes, colors, and dimensions of objects by processing the amount of light they reflect or emit. An eyeball, illustrated in Figure 1.2, consists three concentric layers: the fibrous, the vascular, and the nervous layers (Wolff Eugene, 1948). The fibrous, first layer itself is made up of two part: the posterior part known as the sclera and the anterior part called the cornea. The sclera is a white nontransparent member and the outermost layer of the eye which covers five-sixths of global of the eye. On the other hand, Cornea is the transparent layer located in the front of the eye that allows lights enter the eye like a window. The vascular layer consists of the iris, the ciliary body, and the choroid. The iris is the most anterior part of the vascular layer which controls the amount of light entering the eye in such a way that if the light is bright, the iris closes, narrowing pupil, and when it is dim it opens, dilating pupil (Iqbal et al., 2006). The ciliary body has the different property such as anchoring the lens in place, changing the lens shape by resting the ciliary muscle, and providing nutrition to the vascular ocular tissues. The most posterior part of the vascular layer is choroid that feeds the outer of the retina (Zhu et al., 2011).

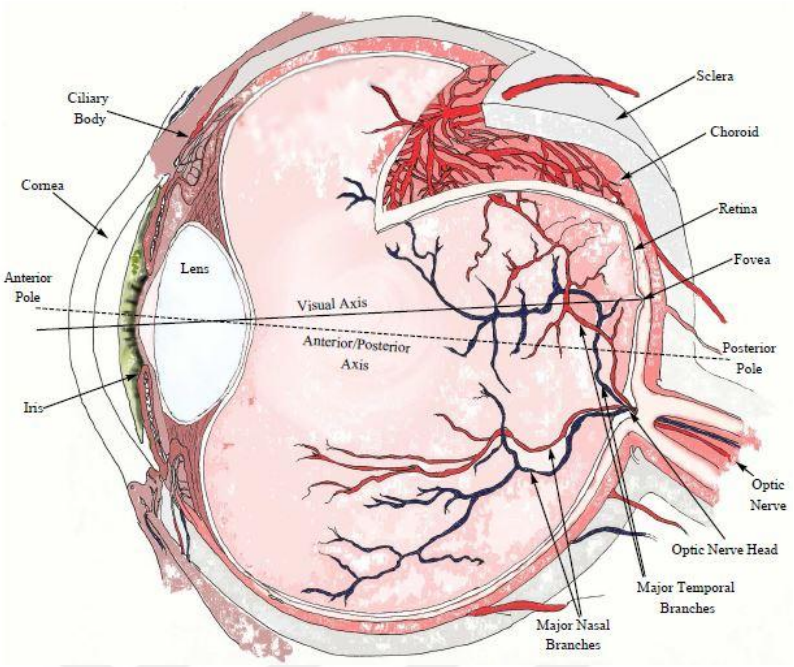

Figure 1.2 Schematic of the sagittal section of the eyeball (Oloumi, 2011).

The retina is a thin layer of neural cells and one of the most important part of the nervous layer. Its thickness is about 0.5mm and lines the inside of the eyeball (Iqbal, 2006). The important point that could be referred is that retina is the only part of nervous system that can be imaged directly. Rods and cones are photoreceptor cells of the retina which receive visual information from the incoming light, encoding corresponding information into the neural signals, and transmit them to the brain for further processing. The corresponding signals are transferred to the brain through the optic nerve head, optic disc. The average diameter of the optic disc is about 1.6mm (Larsen 1976). The major vein and artery branches of the retinal blood vessels diverge away from the stem of the optic disc into the retina. Smaller blood vessels branch off from the parent branch and converge toward a region called the macula, at the center of which is an avascular spot called the fovea. The width of retinal blood vessels changes from 50 to 200µm, 60µm median, in 2-D retinal fundus images (Patton et al., 2006). The macula is located about 3.2µm to the center of the optic disc along the retinal raphe. Retinal raphe has known as the straight line which goes through the center of the optic disc and the fovea. The retinal raphe divides area into two parts. The first part, the area above the retinal raphe is called the superior side

and the second part, the area belows the retinal raphe is called inferior side (Oloumi, 2011). Figure 1.3 shows a typical retina fundus image from DRIVE database. As can be seen, the macular area located in the black circle near the middle of the image appears darker than the background area and the fovea, black dot in the middle of the circle, become visible as a small bright spot in the middle of the macula. The black dot in the right region of the image indicates the center of the optic disc, the point of convergence of retinal blood vessels. The other important point is that the major venule branch is thicker than the corresponding arteriole and has higher background contrast. The inferior major vein/artery is also labeled in the corresponding figure.

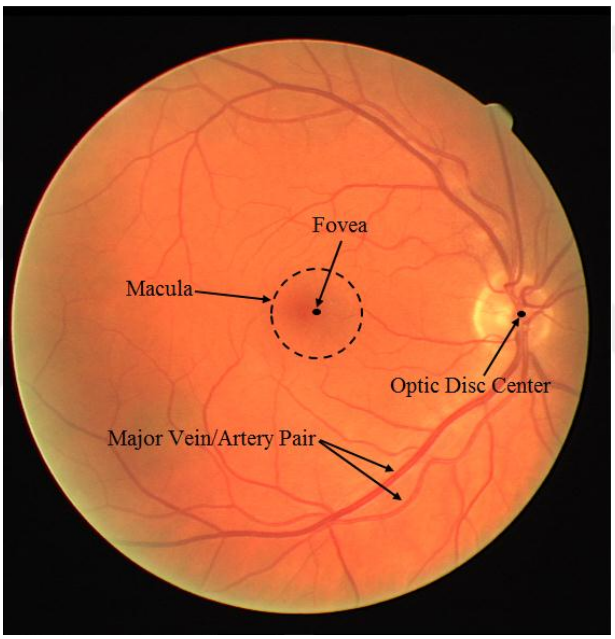

Figure 1.3 Image 24 of the DRIVE database.

1.2 Pathologies of the Eye

With regarding structure of the retina and the fact that the retina is an active tissue, many important diseases related to the eye, brain or the cardiovascular system can show themselves in the retina. In this section, a brief summary of corresponding diseases is given.

1.2.1 Diabetic Retinopathy

Diabetic retinopathy (DR) is one of the most common cause of blindness and visual loss in the people of working age. DR is a result of diabetes mellitus which affects the retinal vasculature and damages the retinal structure. According to the current definition from the world health organization, diabetes mellitus is known as a disease under the condition that a patient has a fasting plasma glucose over 7.0 mmol/l. This can lead to damage major blood vessels, kidneys, heart, brain and eye and results in a retinal complication of diabetes called diabetic retinopathy (Laud, & Shabto, 2010).

There are two different kind of pathological changes in the retina due to DR; ischemia and blood vessel wall damage. When the retina become ischemic, the new blood vessels start to grow in areas of the retina which may subsequently bleed and cause retinal detachment, a condition called proliferative diabetic retinopathy (PDR) (Kanski, & Bowling, 2011). Another complication of DR is retinal blood vessel wall damage which lead to blood and fluid to leak on the retina, a condition called diabetic macular oedema (DME). According to the pathology of DME, this forms different features such as micro-aneurysms, haemorrhages, exudates and cotton-wool spots (Browing, 2010). Figure 1.4 illustrates different kinds of Symptoms of DR in retinal fundus images.

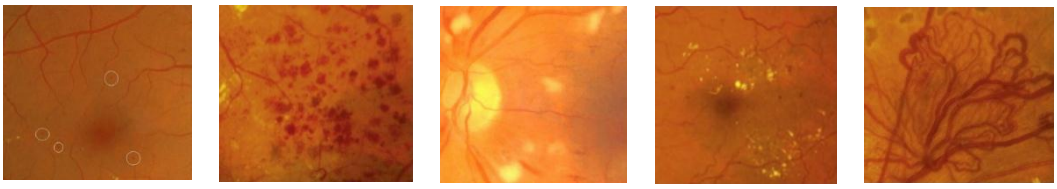

(a) (b) (c) (d) (e)

Figure 1.4 Symptoms of DR in retinal fundus images. a) Micro aneurysms b) Dot and blot haemorrhages c) Soft exudates d) Hard exudates e) Formation of new vessels in retina (Kanski, & Bowling, 2011).

1.2.2 Age Related Macular Degeneration

Another most common cause of visual loss is age-related macular degeneration (AMD). According to the world health organization, AMD is a growing public health problem in most of developed countries. There are different signs of AMD such as drusen information, pigment changes, atrophy and choroidal neovascularization (CNV). Drusen is the small yellow deposits in the macula, also known as the earliest sign of AMD. Pigment changes in the macula is another important sign of AMD. The macular pigment can wither away in a process called atrophy (Chiang et al., 2011).

There are two different types of AMD; dry and wet. Most of the people how have AMD, around 90%, have the dry form of AMD which typically leads to gradual loss of visual acuity. Drusen information, pigment changes, and atrophy are known as dry AMD. A few percent of people, around 10%, with AMD, have wet form of AMD. Wet AMD also known as CNV occurs when abnormal blood vessels develop underneath the macula which leads to leaking fluid and blood and finally cause scarring of the macula (Kanski, & Bowling, 2011). Figure 1.5 shows different signs of AMD in retinal fundus images.

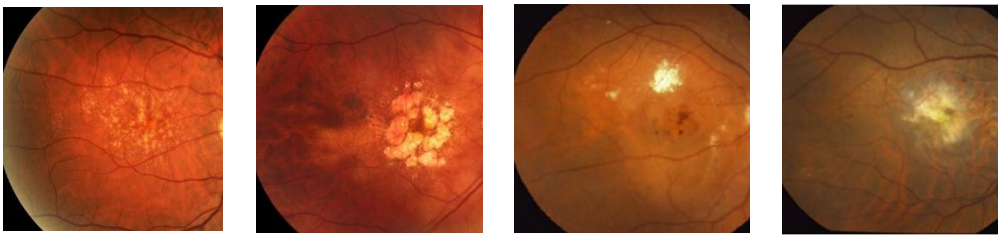

(a) (b) (c) (d)

Figure 1.5 Symptoms of AMD in retinal fundus images. a) Dry AMD with drusen b) Dry AMD with atrophy c) Wet AMD with haemorrhages d) Wet AMD with macular scaring (Fraz, 2013).

1.2.3 Glaucoma

Glaucoma is specified by damaging of ganglion cells and their axons in the retina. It is primarily a neuropathy, not a retinopathy, which results in the cupping of the

optic disc as shown in Figure 1.6. One of the most important indicators for assessing the presence of glaucoma is the cup to disc ratio. This ratio is equal to the ratio of optic disc cup and neuro-retinal rim surface area (Strouthidis, & Garway, 2009).

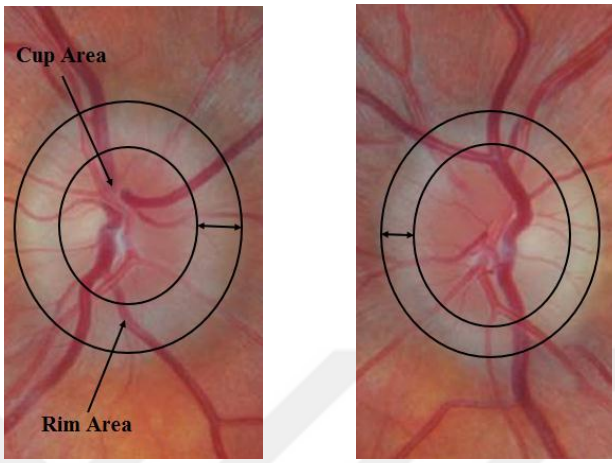

(a) (b)

Figure 1.6 Symptoms of glaucoma in retinal fundus images. a) Normal optic disc b) Glaucoma effected optic disc.

1.2.4 Cardiovascular Disease

The appearance of the cardiovascular disease in the retina is seen in several ways. The changes in the ratio between the diameter of retinal arteries and veins, also called A/V ratio, is specified in the case of hypertension and arteriosclerosis. There is special dependence between changing the A/V ratio and risk of stroke in such a way that a decrease in the A/V ratio, i.e. thinning of the arteries and widening of the veins is associated with an increased risk of stroke (Wong et al., 2002). The direct retinal ischemia can be also invoked because of hypertension which results in the retinal infarcts visible as cotton wool spots and choroidal infarcts visible as deep retinal white spots. Moreover, systemic vascular disease can result arterial and venous occlusions, also called central and branch arterial occlusions (CRAO, BRAO) and central and branch venous occlusions (CRVA, BRVO) (Kanski, & Bowling, 2011).

1.2.5 Retinopathy of Prematurity

Retinopathy of prematurity (ROP) is one of the most common cause of blindness in both adults and especially children which can be diagnosed and treated by laser surgery at early stages. The intensity of ROP can be classified by the presence of plus disease. Diagnosis of the plus disease is made by visual qualitative comparison to a standard photograph of fundus of the retina which make the definition of the plus disease difficult in the quantitative manner (Wilson et al., 2008). Changes in vessel thickness and tortuosity are important signs of the plus disease. According to the literature, there is a direct relationship between increasing the thickness and increasing the intensity of ROP and the plus disease. Moreover, tortuosity of blood vessels has shown the higher correlation with the presence of plus disease. The important point that should be referred is that the detection of small changes in vessel width and tortuosity require high-resolution images (Heneghan et al., 2002). Figure 1.7 illustrates an example of retinal fundus image with tortuosity in blood vessels.

Figure 1.7 Image 198 from STARE database: tortuosity in retinal blood vessels.

1.3 Computer Analysis of Retina for Diagnosing of Diseases

Developing an automatic computer system for diagnosis of retinal diseases is an important task at health-care centers around the world. There are so many advantages of using a computer system for diagnosis several diseases in the retina by image processing techniques and pattern recognition methods such as reducing the workload, providing objective decision-making tools to ophthalmologists, facilitating precise measurement of difficult parameter and quantifying small changes in the measurements (Patton, 2006). It was proved that corresponding systems can detect several pathologies mentioned in section 1.2 which can then results in early treatment. In the most of automatic computer systems, the main features of retina such as blood vessels, optic nerve head, and area of macula should be segmented as an initial step of analyzing the retinal images and the other features like diameter of the blood vessel, tortuosity of blood vessels, and the positions of lesions can then be measured and detected automatically as a further processing for diagnosing AMD, DR, ROP and other pathologies conditions.

Segmentation and analysis of the retinal blood vessels, retinal vasculature, plays an important role in further analysis of retinal images such as the implementation of screening program for DR (Teng et al., 2002), foveal avascular region detection (Haddouche et al., 2010), the evaluation of retinopathy of prematurity (Heneghan et al., 2002), arteriolar narrowing detection (Grisan, & Ruggeri, 2003), the determination of relationship between vessel tortuosity and hypertensive (Foracchia, 2001), measurement of vessel diameter to diagnosis cardiovascular and hypertension diseases (Lowell et al., 2004), computer-assisted laser surgery (Pinz et al., 1998), identification of optic disc position (Hoover, & Goldbaum, 2003), localization of the fovea (Huiqi, & Chutatape, 2004), retinal image mosaic synthesis (Fritzsche et al., 2003), tracking the optic nerve head in video sequences (Solouma et al., 2002), and e.t.

Manual detection of retinal blood vessels and measurement the several properties of extracted vessels such as width and tortuosity is very difficult and time consuming

task which can also requires training and skill. Therefore, the automatic segmentation and quantification of retinal vessels is confirmed by the medical community as an initial step in the development of automatic computer system assisted diagnostic system for ophthalmologic disorders.

1.4 Organization of Thesis

The thesis includes five chapters. Chapter 2 describes the literature and background related to the vessel segmentation methods, width and tortuosity measurement algorithms. In chapter 3 a supervised method is introduced for extraction the blood vessel network by using an ensemble classifier. In the following chapter an automatic algorithm is presented for measuring the diameter and tortuosity of blood vessels and the results of the corresponding measures is analyzed to extract meaningful information for pathological purpose. Finally, chapter 7 discusses the conclusions and recommendations for future work.

CHAPTER TWO
BACKGROUND AND LITERATURE

2.1 Literature Overview

In this chapter, a brief review of retinal vessel segmentation techniques, width and tortuosity measurement methods are presented. Moreover, the advantages and disadvantages of corresponding approaches are discussed. The goal is to present a detailed resource of corresponding algorithms as a ready reference. This chapter begins by introducing the details of the publicly available databases, DRIVE and STARE, of retinal images and the quantitative measures of performance for vessel segmentation.

2.2 Database of Retinal Images

The proposed methods for retinal vessel segmentation, width and tortuosity measurement are tested with the two most popular and online available database of retinal fundus images from the DRIVE and the STARE database. A brief overview of the details of corresponding databases is presented in this section.

2.2.1 The DRIVE Database

The DRIVE (Digital Retinal Images for Vessel Extraction) database which is collected by Niemeijer et al. (2004) was gathered from a DR screening program in Netherland. This database consists of 40 images, 33 without any abnormal sign and 7 with signs of mild DR, captured by a Canon CR5 3CCD camera with a 45^0 field of view (FOV). The size of each image is 768×584 pixels with 8 bits per color channel and the FOV is circular with 450 pixels in diameter. The format of all images is JPEG (Joint Photographic Expert Group). These 40 images are divided into equal groups, training and testing, which make this dataset very useful for supervised methods. All of the images have been segmented manually as a ground truth and FOV binary masks are also provided for all of them. The images in training set were

segmented once, while the images in testing set were segmented twice which result in two groups A and B. In set B, 12.3% of pixels were segmented as vessels against 12.7% for set A. The performance of our vessel segmentation algorithm is measured on the test set using the segmentation of set A as a ground truth. Figure 2.1 shows an example of retinal fundus image of DRIVE database and the related ground truth and FOV mask for corresponding image.

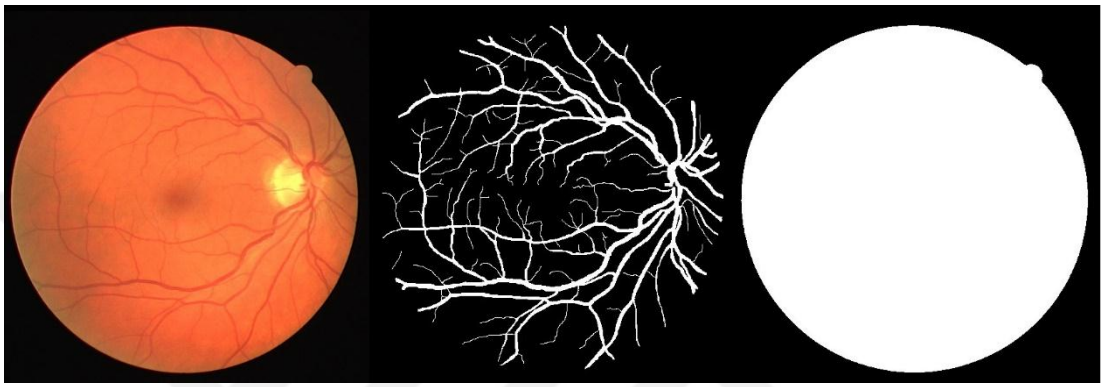

(a) (b) (c)

Figure 2.1 Retinal fundus image 02 from test set of the DRIVE database. a) original RGB image b) manual segmentation of blood vessels known as a ground truth c) the FOV mask of the corresponding image.

2.2.2 The STARE Database

The STARE (Structured Analysis of the Retina) database collected by Hoover et al. (2000), includes 20 images, 10 with pathologies and 10 without any pathologies. All images were captured by a TopCon TRV-50 fundus camera at 35^0 FOV. The size of each image is 700×605 pixels with 8 bits per color channel and the FOV in the images is approximately 650×550 pixels. Two observes manually segmented all of the images as a ground truth. The first observe segmented 10.4% of pixels as vessels against 14.9% for the second observe. The performance of our vessel segmentation algorithm is measured by using the segmentation of the first observe as a ground truth. There are no available FOV binary masks for this database, but we follow the approach in Azzopardi et al. (2015) to create FOV binary mask for each image by thresholding the luminosity plane of Lab version of the original RGB image. Figure

2.2 illustrates an example of retinal fundus image of STARE database and the related ground truth and FOV mask for corresponding image.

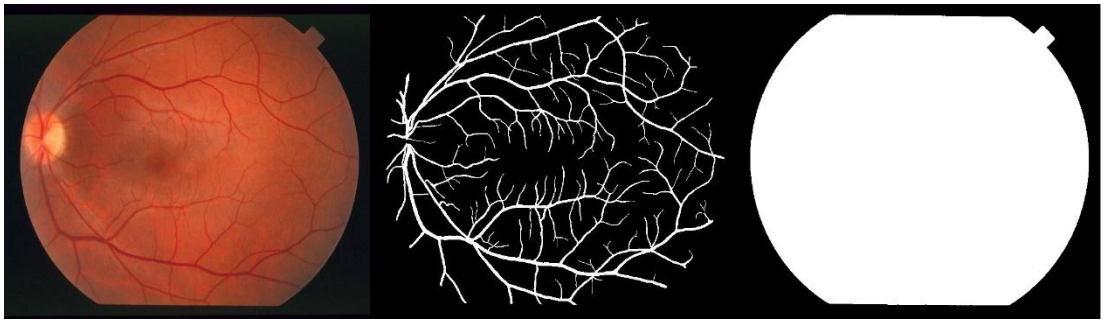

(a) (b) (c)

Figure 2.2 Retinal fundus image 0255 from the STARE database. a) original RGB image b) manual segmentation of blood vessels known as a ground truth c) FOV mask of the corresponding image.

2.3 Performance Measures

In the result of retinal blood vessel segmentation methods, each pixel is classified as vessel pixel or background pixel. With regard to this fact, there are four possibility: two classifications and two misclassifications which can be seen in Table 2.1. the two classification ones are true positive (TP) and true negative (TN), the TP means a pixel is classified as vessel and it is vessel also in ground truth, the TN means a pixel classified as a background pixel and it is a background pixel in ground truth correctly. As for the misclassification, the false negative (FN) means a pixel is classified as background pixel in segmentation result but it is a vessel pixel in ground truth and the false positive (FP) means a pixel is classified as a vessel pixel, but it is a background pixel in ground truth.

Table 2.1 Vessel classification

	Vessel (Ground truth)	**Nonvessel (Ground Truth)**
Vessel (Predicted)	True Positive (TP)	False Positive (FP)
Nonvessel (Predicted)	False Negative (FN)	True Negative (TN)

Due to measure the performance of our method and also for comparing the correspond performance results with other state-of-the-art methods, several metrics are calculated such as accuracy (Acc), sensitivity (SN) and specificity (SP). Acc is one of the most important metrics which equals to the ratio of the total number of correctly classified pixels to the total number of pixels in the image FOV. SN reflects the ability of the algorithm to detect the vessel pixels and SP is the ability to detect non-vessel pixels, background pixels. Moreover, the receiver operating characteristic (ROC) curve is used to measure the performance of proposed method. An ROC curve is a plot of true positive rate (TPR) versus false positive rate (FPR) by changing the thresholds on probability map image. One of the most important metrics extracted from ROC curve is the value of the area under the curve (AUC) which is 1 for the best system. It means that the closer the curve approaches the top left corner, the better is the performance of the corresponding system. The important point that should be referred is that for the retina images, all of the metrics are computed considering only the pixels inside the FOV. All of the metrics described are summarized in Table 2.2.

Table 2.2 Performance metrics of retinal vessel segmentation.

Metrics	Measurement
SN	TP/(TP+FN)
SP	TN/(TN+FP)
TPR	TP/Vessel pixel count
FPR	FP/Non-vessel pixel count
Acc	(TP+TN)/(TP+FP+TN+FN)
AUC	Area under the ROC curve

2.4 Retinal Vessel Segmentation Approaches

One of the most important steps in retinal image analysis procedure is the blood vessel segmentation, due to measuring many important properties of blood vessels, such as diameter and tortuosity depend on the accuracy of blood vessel segmentation. In this section, a brief review of previously developed methods and algorithms for detection of the retinal blood vessel is presented. With regarding the literature, there are several automatic methods for segmentation of retinal blood vessels. These methods can be divided in two main category; supervised methods and unsupervised methods.

Unsupervised methods which is called rule-based methods find vessel locations by using presumed rules for vessels. This category itself includes five main subcategories; vessel tracking, matched filtering, morphological processing, multi-scale analysis and model based algorithms.

Vessel tracking methods, (Liu, & Sun, 1993), (Gao et al., 2001), (Chutatape, Zheng, & Krishnan, 1998), (Grisan et al., 2004), in general speaking segment a vessel between two points using local information. In this kind of approaches, by choosing a set of seed points either manually or automatically, the vascular tree is obtained following the vessel center lines. It means that tracking consists of following vessel centerlines guided by local information, usually trying to find the path which best matches a vessel profile model. There are some important advantages of using vessel tracking methods such as, providing highly accurate vessel widths, following a whole tree without wasting time in areas that does not contain vessel, giving information about structure of individual vessel such as branching and connectivity. The main disadvantage of these methods is the failure of the method to detect vessels which have no seed point and also missing and bifurcation points can result in undetected sub-tress. Moreover, these methods are very sensitive to detect the vessels with a central reflex.

Matched filtering techniques, (Hoover et al., 2000), (Gang et al., 2002), (Chaudhuri et al., 1989), (Zhang et al., 2010), (Al-Rawi et al., 2007), are based on the convolution of the two dimension kernel of the Gaussian or its derivatives with the retinal image. The segmentation of blood vessels in these methods carry out by convolving the retinal image with matched filter rotated in the several direction, with recording the maximum response of each pixel. There are three important properties which must be assumed to design the matched filter kernel; vessels may be approximated by piecewise linear segments, the diameter of the vessels decrease as they move outward from the optic disc and the intensity of a vessel can be approximated by a Gaussian curve. This method requires several convolution kernels which are applied in the several rotation for capturing different features in the image and also specifying the standard deviation parameter of Gaussian function is an important task in these methods. Moreover, the number of incorrect responses may increase by using different kernels due to the presence of pathologies and retinal background variation which have same features as the vessels.

Morphological image processing is a technique based on mathematical operations. Structure elements were applied to the image by morphological operators. The important point that should be noticed is that the image which is processed by the morphological operations must be a binary image. There are several important morphological operations such as dilation, erosion, closing and opening. Dilation expands the objects, erosion shrinks the objects, closing is a dilation followed by an erosion and opening is the erosion followed by a dilation. Mathematical morphology operations are firstly used for enhancing the retinal blood vessels and then by combination with curvature evaluation (Zana, & Klein, 2001) and matched filtering for line detection (Mendonca, & Campilho, 2006), (Fraz, & Owen, 2012), is deployed for retinal vessel segmentation. These methods have the advantages of speed and resistance to noise. On the other hand, the disadvantage of these methods is that they do not exploit the known vessel cross-sectional shape. Moreover, the use of inappropriate structure element may cause difficulty in fitting to highly tortuous vessels.

Other unsupervised method based upon scale space analysis is also multi-scale approach techniques, for instance, Martinez et al. (2007), proposed a multi-scale based method for measuring the width, size and orientation information of retinal blood vessels using the first and the second derivative of the intensity along the scale space which give information about the topology of the image. Frangi (1998) introduced the multi-scale method based on the multi-scale second-order local structure of an image, Hessian. A vesselness measure is obtained on the basis of eigenvalue analysis of the Hessian.

Model based approaches are classified in three categories; vessel profile models, active contour models and geometric models. Vessel profile models, (Li, Bhalerao, & Wilson, 2007), (Narasimha et al., 2007), based on the structure of the vessels. For instance, vessel cross-section intensity profiles approximate a Gaussian shape or a mixture of Gaussian in the case of central reflex in blood vessels. There are also other profiles such as second order derivative Gaussian and the cubic spline which can be replaced. Moreover, there are more complex profiles include the non-vessel features like bright or dark lesions and other background features which increase the accuracy of the segmentation. Active contour models, (Al-Diri, Hunter, & Steel, 2009), known as snakes are the curves defined within an image domain that can move under the influence of the internal forces within the curve itself and external forces derived from the image data. The corresponding snake will conform to different features within an image due to the external and internal definition. The internal forces give tension and stiffness features to the behavior of the snake and the external forces are fixed by a supervised process or human user. Geometric models, (Sum, & Cheung, 2008), are performed by especial algorithms known as level-based numerical algorithms. These algorithms are numerical methods for tracking interfaces and shapes.

Supervised methods called pixel feature classification methods are machine learning techniques that assign labels, vessel or non-vessel, to each pixel. Pixel feature classification methods utilizing ground truth data usually consist of two stages: feature extraction and classification. In the first stage different kind of

features of each pixel and its neighborhood such as, Gabor wavelet (Soares et al., 2006), line operators (Ricci, & Perfetti, 2007), vesselness (Frangi et al., 1998), is extracted for further processing. In the next stage, classification stage, each pixel is classified as a vessel or non-vessel using different kind of classifiers or multi-classifiers such as, multilayer neural network (Sinthanayothin et al., 1999), support vector machine (SVM) (Ricci, & Perfetti, 2007), random forest (Cheng et al., 2014), bagging and boosting (Fraz, & Barman, 2012), Bayesian (Soares et al., 2006). Classification stage itself consists of two distinct parts: training, learning, and testing. The algorithm is statistically learned to correctly classify pixels from known classifications in the training stage. Then in the next stage, testing, the algorithm classifies previously unseen pixels. For proper assessment of supervised classification method functionality, training data and performance testing data sets must be completely disjointed (Abramoff, Garvin, & Sonka, 2010).

According to the literature, there are different kinds of supervised methods to segment blood vessels. Soares et al. (2006) utilized supervised classification method for detecting the blood vessels in retinal fundus images by applying different scales of two dimension complex Gabor wavelet in the feature extraction stage and then a Bayesian classifier was used in classification stage. Ricci et al. (2007) proposed a computationally simple but more effective supervised method by using two line operators which have been modified to take into account the peculiarities of retinal vessel structures for computing the feature vectors, while a linear support vector machine (SVM) was chosen as a classifier. Fraz et al. (2012) performed multi feature analysis using the features such as; gradient orientation analysis, morphological transformation with linear structuring element, line strength measures and Gabor wavelet response which encodes information to successfully handle both normal and pathological retinas with bright and dark lesions simultaneously. They used supervised method for the segmentation of blood vessels by a multi-classifier of boosted and bagged decision trees. Lupascu et al. (2010) also performed multi-feature analysis using a feature vector containing 41 features obtained at different scales to train a classifier which was then applied to the test set. All of these features in further processing were used for classification using an Ada boost classifier. Staal

et al. (2004) used a system that is based on extraction of image ridges as feature, which coincide approximately with vessel centerlines and then the corresponding features were used for classification using a *k*-nearest-neighbor (KNN) classifier. Cheng et al. (2014) used a supervised method for the segmentation the blood vessels by extracting a set of features and applying local context path to some of them for creating the hybrid feature vector. As a result of the feature extraction more than 200 features were extracted and then a random forest classifier by taking advantage of its strong discriminative power and its flexibility of fusing heterogeneous features was used for classification stage.

2.5 Retinal Vessel Width Measurement Algorithms

Accessing the accurate value of blood vessels width is one of the ultimate goal of the retinal blood vessel analysis due to the diameter changes in retinal blood vessels are important factor of presence of many diseases such as plus diseases, diabetic mellitus and cardiovascular diseases, as described in section 1.2. According to the literature, there are many different methods for measuring the diameter of the retinal blood vessels which most of them based on the idea of measuring a vessel perpendicular to its local longitudinal orientation.

Brinchmann-Hansen et al. (1986) introduced a method called Full Width Half Maximum (FWHM) for measuring blood vessel width from an intensity profile orthogonal to a retinal blood vessel. FWHM method is based on the recognizing the minimum and maximum intensity levels on either side of initial estimated mid-point of the profile. Using the mean value of the maximum and minimum points on the left and right side of the profile the half maximum is determined. The width is then estimated by measuring the distance between the half maximums. Another method which is proposed by Gregson et al. (1995) consists of a rectangle profile with a fixed height that is fitted to the profile data. In order to measure the value of the high of the corresponding rectangular the minimum value of the intensity subtracted from the maximum value of the intensity. The width of the rectangular profile is then manipulated until the area under the rectangular profile is equal to the area under the

profile data. Lowell et al. (2004) proposed an algorithm for measuring retinal blood vessel width by fitting a two-dimension model on green channel of original RGB fundus retinal image. The corresponding method looks like an idealized cross section profile running along the length of the vessel in a small region. Al-Diri et al, (2009) introduced a technique for segmentation and measurement of retinal blood vessels based on the Ribbon of Twins active contour model which two pair of contours were used to achieve each vessel edge. Most recently, an algorithm is proposed by Nguyen et al. (2013) to segment retinal blood vessel and measure the diameter of segmented blood vessels. In the corresponding method after segmentation of the retinal blood vessels obtained, the pair of edge points around the specific center point identified. The distance between these two edge points is considered as a vessel width at the corresponding center point.

2.6 Retinal Vessel Tortuosity Measurement Algorithms

According to the recent developments in medical image processing techniques, several features in retinal vasculature have identified. One of these important features is retinal vascular tortuosity. Normal retinal blood vessels are straight, however, they became tortuous in the presence of several diseases such as, plus diseases as referred in section 1.2. With regarding the literature, there are several different methods for measuring the retinal vasculature tortuosity.

The simplest and the most widely utilized method, known as arc length over chord length ratio, is firstly proposed by Lotmar et al. (1979) for measuring the vessel tortuosity. This method provides a simple measurement under the assumptions that the non-tortuous vessels are straight line and the radius of curvature is much larger than the chord. Hart et al. (1997, 1999) proposed a number of methods for tortuosity measurement includes the integral of the absolute curvature, squared curvature integral, the ratio between the absolute curvature integral (or the squared curvature integral) and chord length (or vessel length). Mean direction angle change is a method that is proposed by Chandrinos et al. (1998). This method is based on the local direction variation of the vessel. Goh et al. (2001) introduced a method based

upon the local direction variation called absolute direction angle change for measure vessel tortuosity. In this method the local direction change is measured for each center point of a vessel and the tortuosity then is computed as the number of times the corresponding angel at each center point is above the fixed threshold. Inflection count metric method for measuring the tortuosity of vessel is proposed by Bullitt et al. (2003). In the corresponding method, Bullitt et al. (2003) claimed that the Lotmar et al. (1979) method may not distinguish between the smoothly curved vessels and vessels that have abrupt changes in their directions. Therefore, a new method based on the number of inflection points (twists) is proposed to overcome the corresponding problem. Grisan et al. (2008) proposed a semi-automated method system to grade tortuosity of retinal vessels. The corresponding method is based on partitioning each vessel in segments of constant-sign curvature and then combining together each evaluation of such segments and their number. Most recently, an algorithm based on the chain code called slope chain code (SCC) was proposed by Bribiesca (2013). In this method, the SCC of a curve is measured by placing straight-line segments of constant length around the curve and calculating the slope changes between contiguous straight-line segments scaled to a continuous range.

CHAPTER THREE
RETINAL VESSEL SEGMENTATION

3.1 Overview of Proposed Method

According to the literature, the important point that should be referred is that supervised methods for retinal vessels segmentation in contrast to unsupervised methods are time-consuming and computationally expensive since different kinds of feature extraction methods and complex classifiers are used for extracting blood vessels. But interesting results have been obtained by pixel classification based on supervised learning on the other hand. The results of blood vessel segmentation in supervised methods in most cases are more accurate than unsupervised methods. Nonetheless there are a number of supervised methods for retinal blood vessel segmentation, automatic segmentation of blood vessels remains as a challenging task due to the presence of numerous problems such as, the variation in vessel appearance, shape and orientations, the low contrast between vasculature and background, the presence of noise, large abnormal regions due to the presence of lesions, exudates and other pathological regions (Ricci et al., 2007). Therefore, it is hard to use a single feature and to address all of these problems.

In this work, we present a supervised method that is based upon the multi-feature analysis of retinal images and using an ensemble random forest (RF) classifier (Breiman, 2001) for retinal blood vessel segmentation. In this section, the summary of the method will be briefly explored. We treat vessel segmentation problem as a pixel feature classification task, in which the most probable class of an unknown pixel, described by a set of its features, is inquired to a machine learning system trained to assign class labels to image pixels. In the first stage of such a method, a feature vector, consisting of different types of strong features, for each pixel in an input image is extracted. The idea behind constructing such a hybrid feature vector is to fuse supportive and complementary local information, provided individually by a set of distinguished feature extraction algorithms, from image data. In the next stage, classification, two classes are considered for each pixel, vessel or non-vessel. A

training set including the pixels that are manually labeled through observation is lined up for the learning stage of the classification. Then, for measuring the performance of the classifier and also for achieving the segmentation of blood vessels in unseen data, a test set is applied to the classifier. We select the RF classifier because of its acknowledged advantages in image analysis applications Figure 3.1 depicts our method in a supervised classification framework

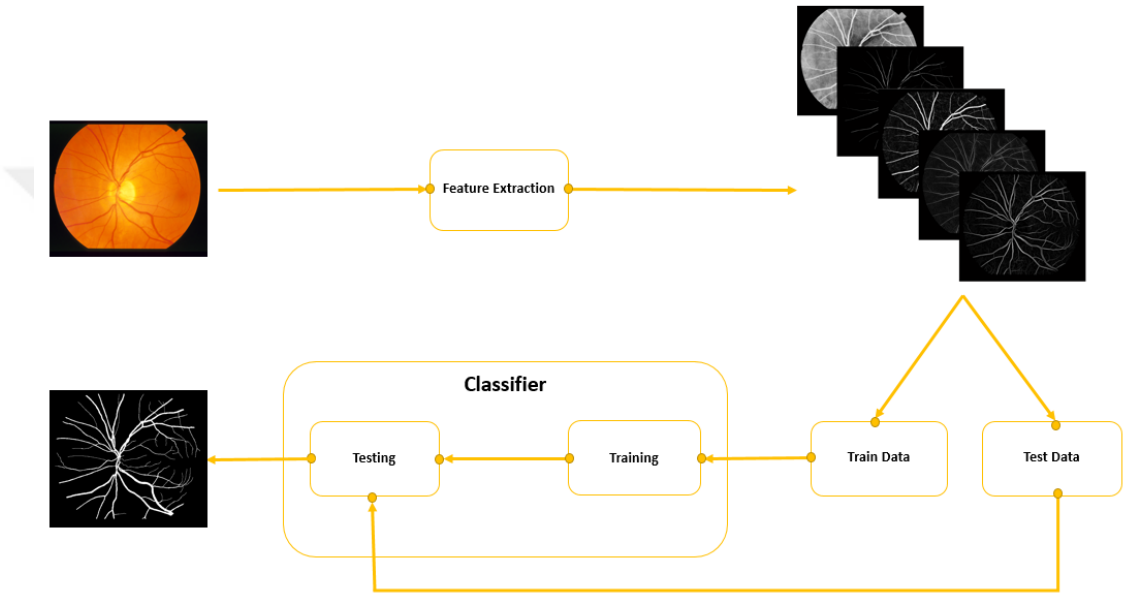

Figure 3.1 General framework of the proposed method for retinal vessel segmentation.

In the following sections, first the different kind of features of each pixel is individually described and then the details of RF classifier algorithm are presented. Consequently, the experimental evaluation of proposed method and a brief conclusion are given in the next sections.

3.2 The Feature Vector

The feature vector containing the quantifiable measurement for each pixel is presented in order to increase the classifier successfully. We have used a heterogeneous set of features to create a robust feature pool. The seventeen dimension feature vector was used which includes the intensity (one feature),

vesselness measure (one feature), morphological transformation (one feature), multi-scale Gabor wavelet (thirteen features), B-COSFIRE filter (one feature). We describe in the following subsections each component of the feature vector.

3.2.1 Intensity Feature

As described in section 2.2, all of the images in both DRIVE and STARE databases are color images represented using the RGB color space. Therefore, each image consists of three scalar valued images; the red, the green, and the blue. Figure 3.2 illustrates the grayscale version for each RGB components. It can be observed that the blood vessels are darker than background in green change than red and blue ones which make the green channel suitable for the purpose of detection of blood vessels.

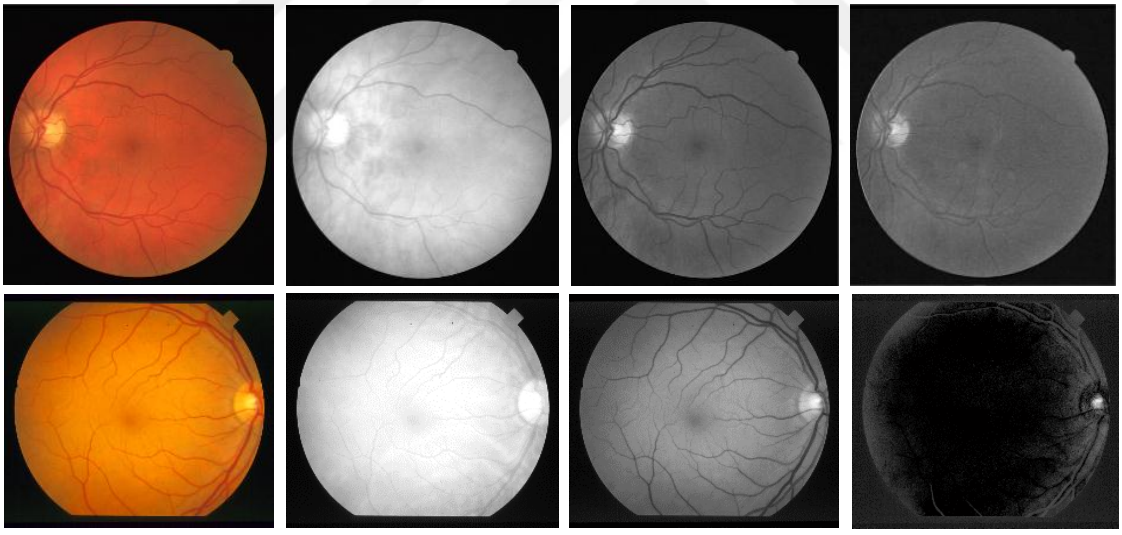

(a) (b) (c) (d)

Figure 3.2 Grayscale representation of image 0082 of the STARE database (second row) and image 05 of DRIVE test dataset (first row). a) original RGB images b) the R c) the G d) the B. It should be noticed that blood vessels have negative contrast all individual channels.

Several methods and algorithms have used the G component for analysis since it provides the best vessel-to-background contrast among the R and the B component. However, it can be claimed that there is still useful information in the G component.

Despite the intensity is an important feature, the enhancing algorithm called contrast limited adaptive histogram equalization (CLAHE) (Pizer et al., 1987) is applied to increase the contrast of blood vessels. CLAHE is a window based enhancement technique which partitions the image into regions and applies the histogram equalization to each one. This process is commonly used as a preprocessing step in most of the analysis of retinal images (Azzopardi et al., 2015) for the improvement of local contrast by avoiding the over-amplification of noise in relatively homogeneous regions. By applying the CLAHE to the intensity image, both bright and dark regions are contrast-enhanced equally well as can be seen in Figure 3.3. In this work, a window size of 8×8 pixels is used. The point that should be referred is that the intensity image enhanced by CLAHE is inverted before using as a feature for further processing.

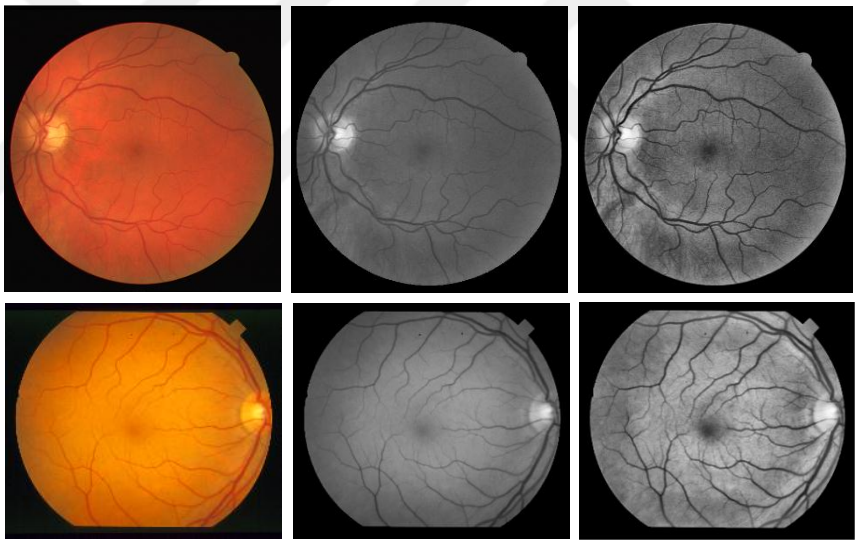

(a) (b) (c)

Figure 3.3 Contrast enhanced images using CLAHE method, first row image 05 from DRIVE database and second row image 0082 from STARE database. a) original RGB images b) intensity images c) images after applying CLAHE method.

3.2.2 Multi-scale Gabor Wavelet

Gabor wavelet is one of the most important filters that is widely used for multi-scale and multi-directional edge detection. In this thesis, we used multi-scale Gabor

wavelet transformation to enhance vessels contrast and filter out the noises. Before extracting Gabor wavelet responses, a preprocessing method including two step is carried out as following. As the first step, the image extending algorithm introduced by Soares et al. (2006) is implemented for removing the border effect of retinal fundus images and reducing the false detection of Gabor filters. This algorithm starts with a region of interest (ROI) specified by the camera's aperture and iteratively grows this ROI. Firstly the set of pixels of exterior border of the ROI is selected, pixels that are outside of the ROI and are neighbors (using four-neighborhood) to pixels inside ROI. Then, the value of each pixel in the corresponding set is replaced with the mean value of its neighbors (using eight-neighborhood). This process is repeated and it can be seen that the ROI is increased as shown in Figure 3.4. As a second step in the preprocessing stage, for increasing the contrast of the blood vessels and the response of the Gabor wavelet filters, the CLAHE algorithm which is explained in section 3.2.1 is applied to the extended image. The result of the CLAHE algorithm can be seen in Figure 3.4.

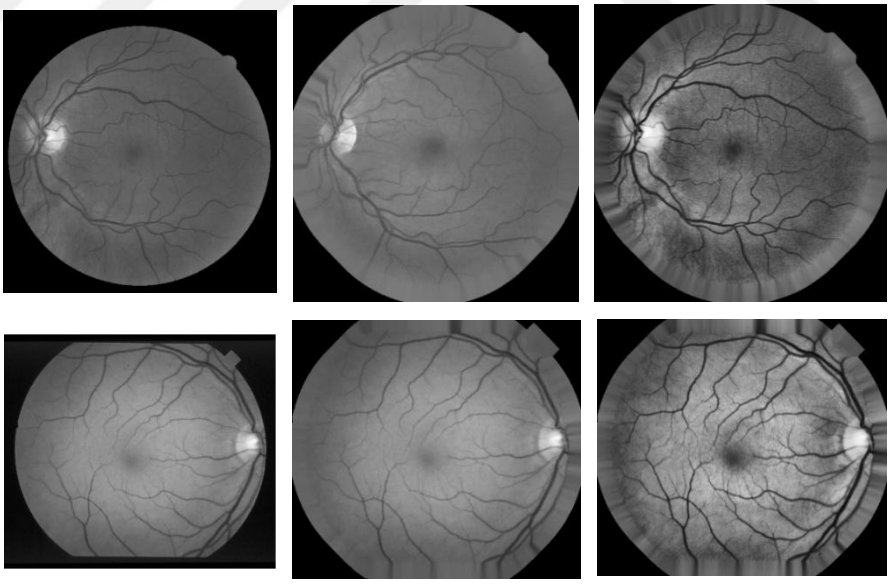

(a) (b) (c)

Figure 3.4 Fundus image preprocessed for removing border effects and enhancing the blood vessels, first row image 05 from DRIVE database and second row image 0082 from STARE database. a) the green channels of colored fundus images b) images with extended border c) the result of applying CLAHE method on extended images.

The Gabor wavelet filter used in our method can be expressed as below;

$$g(\mathrm{X};\lambda,\theta,\sigma,\gamma) = \exp(-\frac{x'^2+\gamma^2 y'^2}{2\sigma^2})\exp(j(2\pi\frac{x'}{\lambda}))$$
$$x' = x\cos(\theta)+\mathrm{y}\sin(\theta) \tag{3.1}$$
$$\mathrm{y}' = -x\sin(\theta)+y\cos(\theta)$$

Where $X=(\mathrm{x},\mathrm{y})$ is a 2-D point, λ represents the wavelength of the sinusoidal factor, θ is the angle of the normal to the parallel stripes of a Gabor function, σ is the standard deviation of Gaussian envelope and γ is the aspect ratio that depicts the elliptic shape by which the Gabor function is supported. The ratio σ/λ, denoted by b, is known as the bandwidth of the Gabor filter. Then, our Gabor filter is parameterized as $G(L;\lambda,\theta,b,\gamma)$. With regarding to each pixel position and considered scale value $(\lambda,\mathrm{b},\gamma)$, maximum response of real, imaginary and magnitude over all orientation was extracted as features as follows;

$$M^c(X;\lambda,b,\gamma) = \arg\max_{\theta\in A}\left\|G^c(X;|\lambda,\theta,\mathrm{b},\gamma)\right\| \tag{3.2}$$

Where $A=\{k\pi/18, k=0,...,17\}$, determined with a relatively small angle step size for a better match to any arbitrary orientation of a vessel point at which the filter is applied, $c\in\{r,i,m\}$, and G^r, G^i, G^m are real, imaginary and the magnitude components of $G(X;\lambda,\theta,\mathrm{b},\gamma)$. Therefore, a Gabor filter bank consisting of multiple scales is applied to the retinal fundus images. The value of the parameters that are specified in our method include, $b\in\{1\}$, $\lambda\in\{2,4,6,8,10,12\}$, $\gamma\in\{0.25,0.5,0.75\}$. So this combination results in 1×6×3=18 different configurations of the filter, and a 54-D Gabor feature vector, considering the real, imaginary and magnitude parts of the filter response. The extended image is inverted before the application of wavelet transformation to it, so that the vessels appear brighter than the background. Such a representation provides positive contrast for the blood vessels, which is required by the Gabor filters used for filtering. An example of Gabor filter response for

$b=1,\ \lambda=6,\ \gamma=0.50$ can be seen in Figure 3.5. The important point that should be noticed is that after applying Gabor filter to the extended image, the corresponding image is converted the same size of ROI.

(a) (b) (c)

Figure 3.5 The Gabor filter response, first row image 05 from DRIVE database and second row image 0082 from STARE database. a) extended image of green channels b) extended image is inverted before applying Gabor filter c) the cropped image of Gabor filter response for scales $b=1,\ \lambda=6,\ \gamma=0.50$.

According to the high dimensionality of the Gabor feature vector for each pixel, 54-D, a feature selection algorithm, correlation-based feature selection (CFS), introduced by Hall et al. (1998) is used as the post processing step to select a subset of features that are highly correlated with the corresponding class. As a result of applying this feature selection algorithm, 13 out of 54 number of features are selected as the best subset for further processing. The interesting point is that all of the features selected by corresponding feature selection algorithm are related to the real part of Gabor filter response. Among the real parts of all responses, a subset specified in Equation (3.3) is also excluded. The feature subset M_s, selected for our method, from the entire Gabor filter responses is given by;

$$\begin{cases} M_s(\mathbf{x};\lambda,b,\gamma) = \left\{ M^r(\mathbf{x};\lambda,1,\gamma) \mid (\lambda,\gamma) \notin B \right\} \\ B = \left\{ (2,\ 0.25),(2,\ 0.5),(2,\ 0.75),(4,\ 0.25),(4,\ 0.75) \right\} \end{cases} \tag{3.3}$$

3.2.3 Vesselness Measure

This is a measure, first proposed by Frangi et al. (1998) based on the eigenvalues of Hessian matrix computed at every pixel in an image. Vesselness measure provides a good enhancement of vessel-like structures in images, using a scale space analysis with Gaussian kernels. The Hessian matrix of image at each point $I(\mathrm{x},\mathrm{y})$ can be calculated by formula below;

$$H(\mathrm{x},\mathrm{y}) = \begin{bmatrix} \dfrac{\partial^2 I}{\partial x^2} & \dfrac{\partial^2 I}{\partial x \partial y} \\ \dfrac{\partial^2 I}{\partial x \partial y} & \dfrac{\partial^2 I}{\partial y^2} \end{bmatrix} = \begin{bmatrix} I_{xx} & I_{xy} \\ I_{yx} & I_y \end{bmatrix} \tag{3.4}$$

Which contains partial derivatives computed by convolving the image $I(x,y)$ with the first derivatives of a Gaussian kernel. The 2-D vesselness measure is defined by below formula;

$$v_0 = \begin{cases} 0 & \lambda_2 > 0 \\ \exp\left(\dfrac{R_B^2}{2\beta^2}\right)\left(1-\exp\left(-\dfrac{S^2}{2c^2}\right)\right) & \text{otherwise} \end{cases} \tag{3.5}$$

Where R_B is the ridgeness score and can be computed by λ_1 and λ_2, eigenvalues of the Hessian matrix in predefined order $|\lambda_1| \le |\lambda_2|$, in such a way that $R_B = \lambda_2 / \lambda_1$ and S is the Frobenius norm of the Hessian matrix;

$$S = \|H\|_F = \sqrt{L_{xx}^2 + 2L_{xy}^2 + L_{yy}^2} = \sqrt{\lambda_1^2 + \lambda_2^2} \tag{3.6}$$

In Equation (3.4), c is equal to half of the maximum Frobenius norm of the Hessian over all Frobenius norms computed on the entire image and we assume $\beta = 0.5$ as Frangi et al. (1998). In the regions containing vessel like structures in an image, the norm value becomes larger compared to the background since at least one of the eigenvalues in those high contrast regions will be large. Because of this fact, the norm of Hessian is used to distinguish between vessel pixels from background. Although the vesselness measure in Equation (3.5) is analyzed at different scales, by varying the spread of Gaussian filter within a range, we select to compute the measure at an optimized single scale. As the number of scales increase, the multi-scale vesselness analysis tends to give a rise in false detections (spurious vessel pixels) in the background region of retinal images. We fix the value of the scale factor in Gaussian filter at 1.5 for both DRIVE and STARE dataset. The example of application of vesselness measure for inverted green channel of colored retinal fundus images can be seen in Figure 3.6.

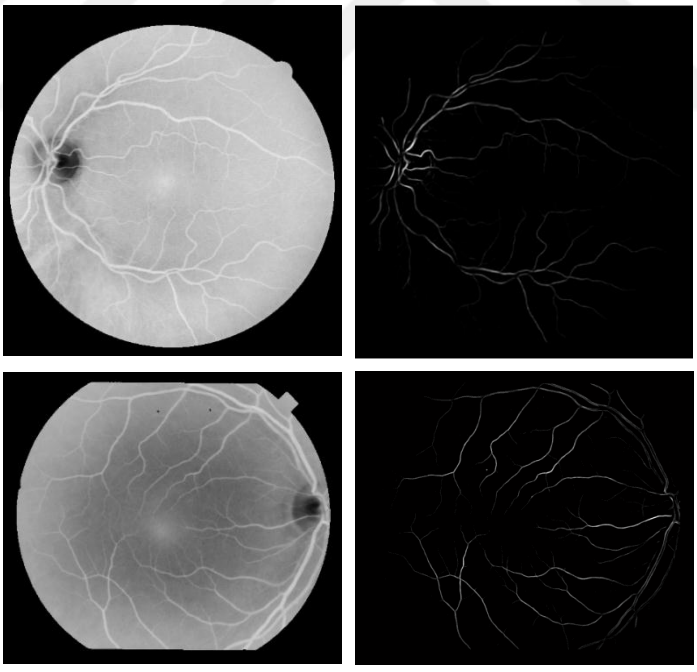

(a) (b)

Figure 3.6 Applying vesselness method on retinal fundus images, first row image 05 from DRIVE database and second row image 0082 from STARE database. a) inverted green channel of colored images b) vessel enhanced images using vesselness measure method.

3.2.4 Morphological Transformation

Morphological top-hat transformation is one of the most important morphological operations and is generally used as a powerful tool in image processing for noise reduction and extracting useful and meaningful information in small regions of images. Structuring element plays an important role in the operation of morphological top-hat transform. For instance, in a blood vessel enhancement application, if a structuring element is not oriented at a suitable angle or is not large enough, a vessel or part of it can be eradicated by the transform. A linear structuring element is rotated at incremental angles through an arc of 180 and the obtained set is applied to image in the morphological opening operations of the top-hat transformations. Morphological top-hat transform is defined by;

$$I_{th}^{\theta} = I - (I \; o \; S_e^{\theta}) \tag{3.7}$$

Where I is the image to be enhanced, I_{th}^{θ} is the top hat transformed image, S_e^{θ} is the structure element, o is the morphological opening operation and θ is the angular rotation of structure elements for morphological opening. A sum of these top-hat transformed images, defined by Equation (3.8), can brighten all of the vessels regardless of their orientation, width, length, and tortuosity as long as the length of the structuring elements is larger than the vessel with the largest diameter.

$$I_{S_{th}} = \sum_{\theta \in A} I_{th}^{\theta} \tag{3.8}$$

A linear structuring element with 21 pixel long (taking into account the diameter of the largest vessel in the databases) and 1 pixel wide, and the rotation at an angle spanning $[0, \pi]$ in steps of $\pi/8$ are selected for opening operations as suggested by Fraz et al. (2012). Therefore, in Equation (3.8), A can be defined as $\{k\pi/8, \; k = 0,1,\ldots,7\}$. The same parameters of the morphological top-hat transformation as referred to above are valid for both DRIVE and STARE datasets. The important point that should be noticed is that the corresponding morphological operation is applied to the green channel of the colored fundus images. The result of

this operation on green channel of colored retinal fundus images can be seen in Figure 3.7.

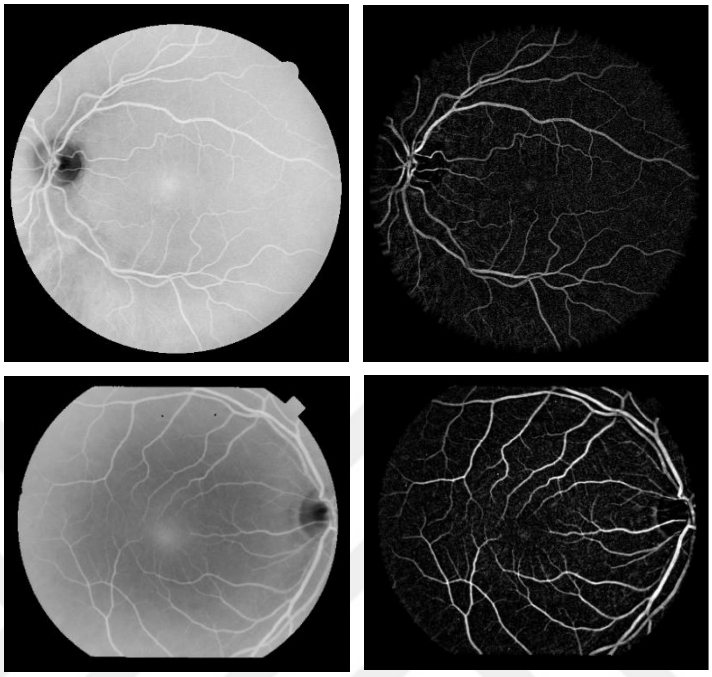

(a) (b)

Figure 3.7 Morphological transformation on retinal images, first row image 05 from DRIVE database and second row image 0082 from STARE database. a) the inverted green channel of colored images b) images after applying morphological operation.

3.2.5 B-COSFIRE Filter

Azzopardi et al. (2015) propose a bar-selective combination of shifted filter responses (B-COSFIRE) to detect bar-shaped patterns in digital images. They successfully detect retinal blood vessels in fundus images by applying their B-COSFIRE filters configured for a prototype bar pattern. A B-COSFIRE filter can be configured to achieve orientation selectivity by multiplying outputs of a group of Difference-of-Gaussians (DoG) filters, whose responses are aligned collinearly. Symmetric and asymmetric B-COSFIRE filters that are selective for bars and bar-endings, respectively, can be configured (Azzopardi et al., 2015) and it is reported

that the best performance can be obtained by summing responses of symmetric and asymmetric B-COSFIRE filters.

Azzopardi et al. (2015) utilized an appropriate DoG filter for detection of intensity changes of retinal images. The corresponding filter is defined by,

$$DoG(x,y) = \frac{1}{2\pi\sigma^2}\exp(-\frac{x^2+y^2}{2\sigma^2}) - \frac{1}{2\pi(0.5\sigma)^2}\exp(-\frac{x^2+y^2}{2(0.5\sigma)^2}) \quad (3.9)$$

Where σ is the standard deviation of the Gaussian function. The response $c_\sigma(x,y)$ of a DoG filter to an image $I(x,y)$ is obtained by convolving the image with $DoG(x,y)$ followed by negative values suppression (setting negative responses to zero). Figure 3.8 shows how to configure a B-COSFIRE filter to detect a vertical bar (or vessel) as prototype pattern. When the DoG filter responses $c_\sigma(x,y)$ along a number of concentric circles around the center point (denoted by '1' in Figure 3.8) of a B-COSFIRE filter are considered, significant responses to dominant intensity changes exist at the points labelled from '1' to '5' (assume a circle of zero radius at the center). The positions of such are points are gathered in a set $S = \{(\rho_i, \phi_i) \mid i = 1,\ldots n\}$ where *n* denotes the number of considered DoG filter responses while ρ_i and ϕ_i represent the polar coordinates with respect to the center point. For the example in Figure 3.8, $S = \{(0,0)_1, (2,\pi/2)_2, (2,3\pi/2)_3, (4,\pi/2)_4, (4,3\pi/2)_5\}$ where each subscript denotes the label of the point for which its position is included in *S*. This configuration process provides a B-COSFIRE filter that is selective for the collinear alignment of significant intensity changes such as vessel-like patterns in an image.

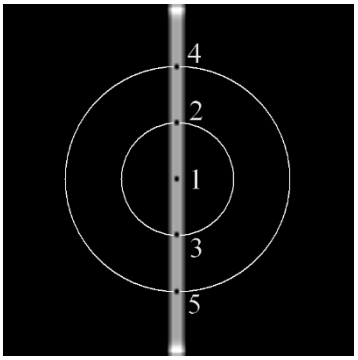

Figure 3.8 Configuration of a vertical bar-selective B-COSFIRE filter. The points with strongest DoG responses along the circles of given radii are labelled by numbers. The filter center point is denoted by '1'.

The output of the B-COSFIRE filter at the center points is computed by using the DoG filter responses in the positions in *S*. The responses in positions (ρ_i, ϕ_i) are brought into the center point after the DoG filter responses are blurred to allow for some tolerance in the position of the concerned points. The blurring is performed by taking the maximum value of the weighted DoG filter responses in a neighborhood of each position (ρ_i, ϕ_i). For the weighting, a Gaussian function $G_{\sigma'}(x, y)$ with variable standard deviation σ' is used, such that $\sigma' = \sigma_0 + \alpha\rho_i$ where σ_0 and α are constants. The blurred and shifted (to the center point) DoG filter response $s_{\rho_i,\phi_i}(x, y)$ in each position (ρ_i, ϕ_i) is defined by,

$$s_{\rho_i,\phi_i}(x, y) = \max_{x', y'}\{ c_\sigma(x - \Delta x_i - x', y - \Delta y_i - y')\, G_{\sigma'}(x', y')\}$$

(3.10)

Where $-3\sigma' \le x', y' \le 3\sigma'$ while the required shift values $\Delta x_i = -\rho_i \cos\phi_i$ and $\Delta y_i = -\rho_i \sin\phi_i$. The weighted geometric mean of all the blurred and shifted responses $s_{\rho_i,\phi_i}(x, y)$ yields the output $r_S(x, y)$ of the B-COSFIRE filter:

$$r_S(x, y) = \left| \left(\prod_{i=1}^{n} \left(s_{\rho_i,\phi_i}(x, y) \right)^{\omega_i} \right)^{\frac{1}{\sum_{i=1}^{n} \omega_i}} \right|_t \qquad (3.11)$$

$$\omega_i = \exp(-\frac{\rho_i^2}{2\hat{\sigma}^2}) \tag{3.12}$$

$$\hat{\sigma} = \frac{1}{3}\max_{i\in\{1\ldots n\}}\{\rho_i\} \tag{3.13}$$

The operator $\left|\cdot\right|_t$ represents thresholding the weighted geometric mean at a fraction t $(0 \le t \le 1)$ of its maximum value. The weighting allows the contribution of the blurred and shifted responses to decrease with an increasing distance from the center point of the B-COSFIRE filter.

A B-COSFIRE filter requires as many blurred DoG filter responses as the number of unique ρ_i values used in the configuration of the filter. For the given configuration in Figure 3.8, only three blurred responses (images) are computed using the Gaussian functions with $\sigma_1' = \sigma_0$, $\sigma_2' = \sigma_0 + 2\alpha$, and $\sigma_3' = \sigma_0 + 4\alpha$. Then, each of the five (*n*=5 in Figure 3.8) different responses $s_{\rho_i,\phi_i}(x,y)$ are obtained by choosing the corresponding blurred response and shifting it by $(\Delta x_i, \Delta y_i)$.

Rotation invariance of a B-COSFIRE filter is achieved by considering $r_S(x,y)$ outputs obtained from a set of configurations for bar prototypes oriented at angles spanning from 0 to π. In order to detect bars at any arbitrary orientation θ_k, a new set $R_{\theta_k}(S)$ is generated from *S* by,

$$R_{\theta_k}(S) = \{(\rho_i, \phi_i + \theta_k) \mid \forall(\rho_i, \phi_i) \in S\} \tag{3.14}$$

The weighted geometric mean of the blurred and shifted responses $r_{S_k}(x,y)$ for orientation θ_k is obtained in the same manner as explained above for $r_S(x,y)$ except that the new set $R_{\theta_k}(S)$ is used instead of *S*. The set of shift vectors $(\Delta x_i, \Delta y_i)$ essentially only differ in computing a new response for a different orientation of the bar. In implementations, 12 angles with equal intervals are used so that $\theta_k = \{k\pi/12 \mid 0 \le k < 12\}$. Thus, rotation invariant response $\hat{r}_S(x,y)$ of a B-

COSFIRE filter can be obtained by taking the maximum responses $r_{S_k}(x,y)$ for $k=\{0,1,..,11\}$ at every position (x,y).

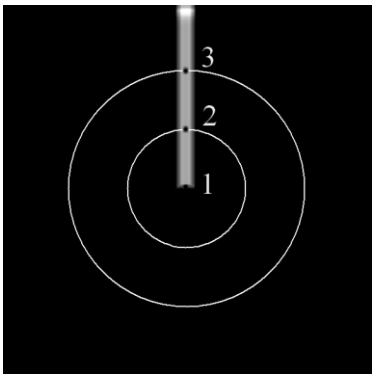

Figure 3.9 Configuration of an asymmetric vertical bar-selective B-COSFIRE filter. The center point of the filter lies on the end of the line.

A B-COSFIRE filter gives much lower response at bar endings than the response that is obtained in the middle of bar. This drawback is overcome by configuring a new B-COSFIRE filter by the prototype bar ending shown in Figure 3.9. The filter center point this time settles on the end of the line and this filter is called asymmetric B-COSFIRE filter in contrast to symmetric B-COSFIRE filter that is described previously. An asymmetric B-COSFIRE filter is much more responsive at the end of a vessel.

We use the summation of responses of symmetric and asymmetric B-COSFIRE filters as a feature in our method. The responses are obtained from the retinal images by setting the parameters (σ, σ_0, α, ρ_i, and t) of both symmetric and asymmetric B-COSFIRE filters as suggested in [28] for the DRIVE and STARE databases. An example of B-COSFIRE filter response can be seen in Figure 3.10.

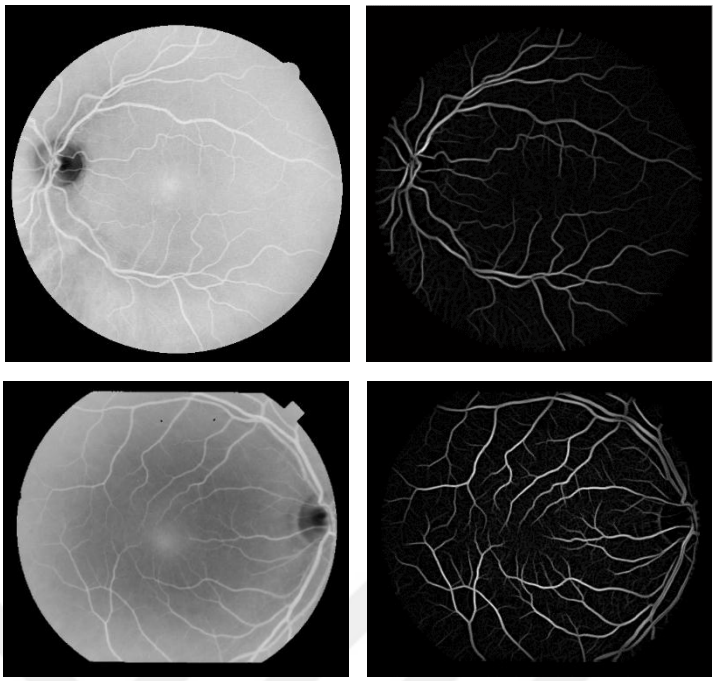

(a) (b)

Figure 3.10 B-COSFIRE filter response on retinal images, first row image 05 from DRIVE database and second row image 0082 from STARE database. a) inverted green channel of colored images b) images after applying B-COSFIRE filter.

3.2.6 Feature Normalization

We have applied the normal transformation known as mean and standard deviation normalization to each feature in such a way that each feature is normalized by its own means and standard deviations which help to compensate for inherent variation between images such as illumination.

For achieving the new variables with zero mean and unit standard deviations in order to reduce the errors in the classification process, the normal transformation is applied to the feature space which is defined in below formula.

$$v_i^{'} = \frac{v_i - \mu_i}{\sigma_i} \tag{3.15}$$

Where v_i is the i^{th} feature, μ_i is the average value of the i^{th}, and σ_i is the standard deviation.

3.3 Ensemble Classification

Ensemble learning methods are an approach used to improve the performance of learning. The main principle of ensemble learning methods is the combination of the weak group of learners to create a strong learner for solving particular machine learning problems. The most important advantages of using ensemble systems are the reduction of variance and an increase in confidence of the decision.

Random forest (RF) is an ensemble method that is very suitable for nonlinear classification in high dimensionality space. RF classifier is based on a learning technique known as decision trees with each tree is constructed via some randomized configuration. The advantage of this randomized configuration is that firstly it makes the classifier very flexible when a large number of heterogeneous features are available since it choose only a subset of features in each tree node. Secondly it makes the classifier useful if there is a huge number of samples available in training stage by selecting a random subset of whole training dataset in each tree. Other benefits of using RF is the easy selection of parameters and the training time is fast.

According to the fundamental of decision trees, there are two different types of nodes in each tree: leaf node which encodes the class distribution for samples that reach it and internal nodes which perform the binary test to split the samples to its child node. The splitting process continuous until a leaf node is reached. A stump can be used to select the best threshold to split samples for minimizing the miss-classification error. The important point that should be noticed is that at each leaf node the posterior probability is learned as the proportion of the training samples labeled as vessels at the corresponding leaf node. In the testing step, the feature of each pixel is first fed into the root of each tree and then it follows the splitting rule until it reaches a leaf. Each tree returns a posterior probability that **x** belongs to a

vessel. The mean of leaf distributions from all trees is used for the final decision. Specifically, the probability that **x** is a vessel pixel is estimated by:

$$Pr(\text{vessel} \mid \mathbf{x}) = \frac{1}{T} \sum_{t=1}^{T} p_t(\text{vessel} \mid \phi(\mathbf{x})) \tag{3.16}$$

Where P_t is the output from the t^{th} tree, T is the number of trees in the forest and $\phi(\mathbf{x})$ is feature of a pixel **x.**

The parameters of RF can be manipulated to achieve the best result of performance. These parameters include; the number of trees, the training dataset sample size for building each decision tree and a number of random features which determine the partitioning of the training dataset at each node.

3.4 Experimental Evaluation

The proposed method has been evaluated using two groups of the online available database, DRIVE and STARE. For measuring the performance of the algorithm, several metrics is measured such as sensitivity, specificity, accuracy, positive predictive value and area under ROC curve. The detail of the metric is described in section 2.3.

3.4.1 Implementation Detail

As described in section 2.2, DRIVE database consists 40 images that are divided into two subsets, training set and testing set. The training set which includes 20 images was used to train the classifier such a way that 300,000 samples, pixels, were randomly selected from corresponding images, 15000 per image. The performance of the proposed method for blood vessel segmentation is measured on the testing set.

Because of the STARE database which includes 20 colored retinal images does not have any separate training and testing sets, different kinds of methods were

utilized to implement the classifier training and testing stages, for instance, Ricci et al. (2007) and Cheng et al. (2014) randomly selected 0.5% and 6% of samples of the entire dataset for training the classifiers and for performing the test stage, all of the images with entire pixels was used. Soares et al. (2006) and Staal et al. (2004) implemented leave-one-out algorithm in this dataset in such a way that every image is classified by using samples from the other 19 images. We followed the method that is implemented by Ricci et al. (2007) on this dataset. We used 60,000 manually segmented pixels which are randomly selected form 20 images, 3000 per image, for training the classifier on this dataset. Due to the small size of training set, 1% of the entire dataset, the performance was evaluated on the whole set of 20 images. The important point that should be referred is that the only pixels located inside the FOV was used for all of processing.

A Random forest classifier was constructed for classification using 150 decision trees in which each decision tree is of depth 15 and built in parallel fashion and also 5 out of 17 features are randomly selected to train an internal node. The output of classifier is a vessel probability map obtained by the voting of all the trees. Accordingly, a simple threshold ($0 \le T_{th} \le 1$) is applied to the probability map for achieving the vessel segmentation. For measuring the performance of results as a further process, the value of threshold must be the same for all images in each dataset. We selected the optimal threshold value for both DRIVE and STARE as $T_{th} = 0.60$.

3.4.2 Vessel Segmentation Results

Binary vessel segmentation image is obtained by threshold the probability map image. All of the performance metrics are computed regarding the first human observer as ground truth. Performance results for individual image in each database can be seen in Tables 3.1 and 3.2.

Table 3.1 Performance results on DRIVE database images. The best case, the worst case and the average value of metrics is highlighted.

Image	SN	SP	ACC	AUC
1	0.7965	0.9759	0.9524	0.979
2	0.8035	0.9795	0.9531	0.979
3	**0.7106**	**0.9760**	**0.9374**	**0.960**
4	0.7653	0.9824	0.9535	0.964
5	0.7524	0.9816	0.9505	0.960
6	0.7227	0.9799	0.9436	0.958
7	0.7308	0.9827	0.9494	0.959
8	0.6814	0.9807	0.9431	0.959
9	0.7540	0.9805	0.9539	0.967
10	0.7477	0.9802	0.9524	0.966
11	0.7350	0.9800	0.9482	0.958
12	0.7698	0.9762	0.9504	0.970
13	0.7439	0.9777	0.9445	0.965
14	0.7808	0.9761	0.9530	0.976
15	0.7766	0.9800	0.9589	0.972
16	0.7553	0.9832	0.9533	0.975
17	0.7134	0.9806	0.9476	0.961
18	0.7424	0.9820	0.9544	0.974
19	**0.8302**	**0.9878**	**0.9688**	**0.982**
20	0.7789	0.9798	0.9584	0.980
Average	**0.7545**	**0.9801**	**0.9513**	**0.9682**

Table 3.2 Performance results on STARE database images. The best case, the worst case and the average value of metrics is highlighted.

Image	SN	SP	ACC	AUC
1	0.7640	0.9661	0.9441	0.971
2	0.6593	0.9861	0.9562	0.963
3	0.7006	0.9850	0.9618	0.974
4	0.6868	0.9833	0.9531	0.968
5	**0.6547**	**0.9758**	**0.9362**	**0.966**
6	0.7641	0.9851	0.9657	0.984
7	0.8436	0.9831	0.9678	0.989
8	0.8355	0.9829	0.9679	0.990
9	0.8463	0.9842	0.9694	0.989
10	0.6991	0.9852	0.9538	0.979
11	0.7953	0.9848	0.9662	0.986
12	**0.8750**	**0.9874**	**0.9763**	**0.992**
13	0.8246	0.9804	0.9614	0.986
14	0.8168	0.9847	0.9638	0.987
15	0.6916	0.9880	0.9548	0.975
16	0.7496	0.9784	0.9464	0.973
17	0.8164	0.9845	0.9638	0.985
18	0.7643	0.9921	0.9762	0.979
19	0.7261	0.9899	0.9743	0.982
20	0.5977	0.9871	0.9516	0.961
Average	**0.7556**	**0.9837**	**0.9605**	**0.9789**

The best case in DRIVE database includes the values 0.9688, 0.8302, 0.9878, and 0.9820 for the accuracy, sensitivity, specificity, and AUC, respectively, the worst case measures are, 0.9374, 0.7106, 0.9760, and 0.9600. Regarding the STARE database, the best case includes the accuracy value of 0.9763, sensitivity, specificity,

and AUC are 0.8750, 0.9874, and 0.9920. The worst case accuracy is 0.9362, sensitivity, specificity, and AUC are 0.6547, 0.9758, and 0.9660. Vessel segmentation result for the best and the worst case in DRIVE and STARE database are illustrated in Figure 3.11 and Figure 3.12.

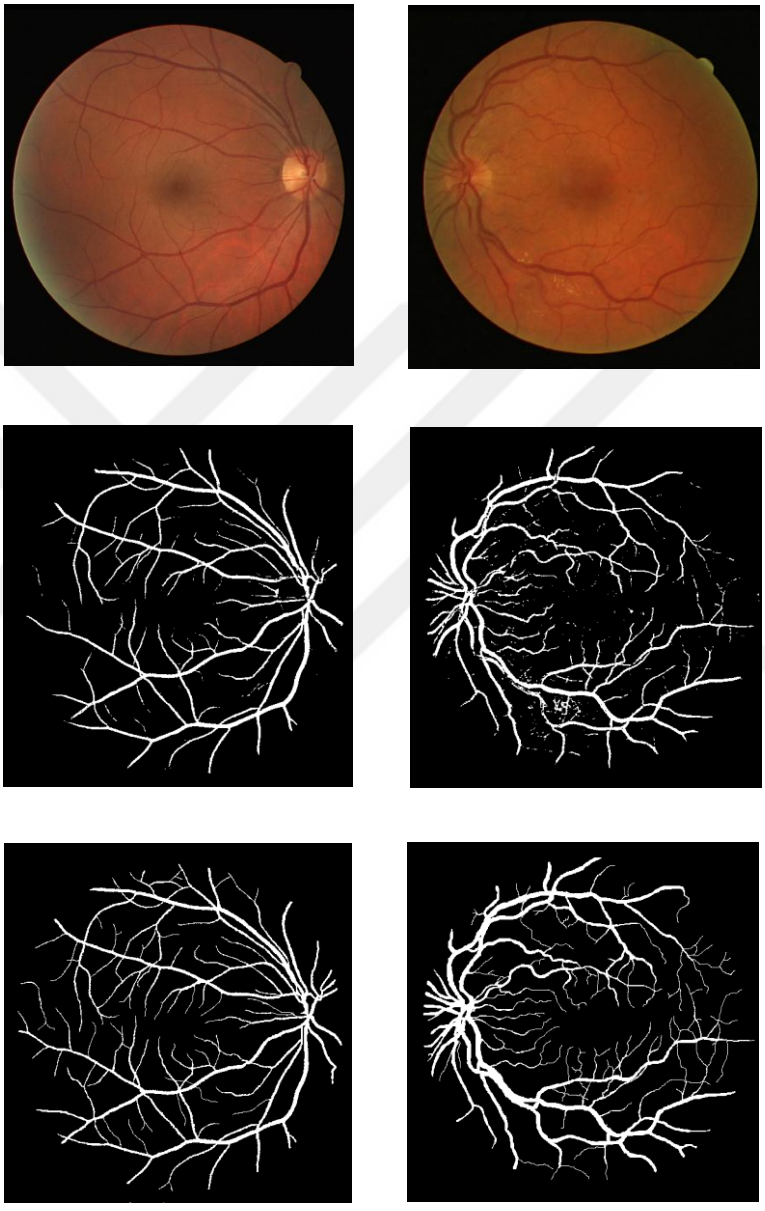

(a) (b)

Figure 3.11 Segmentation results for DRIVE database, first row: Input images, second row: segmentation results, third row: first human observer. a) best case accuracy b) worst case accuracy.

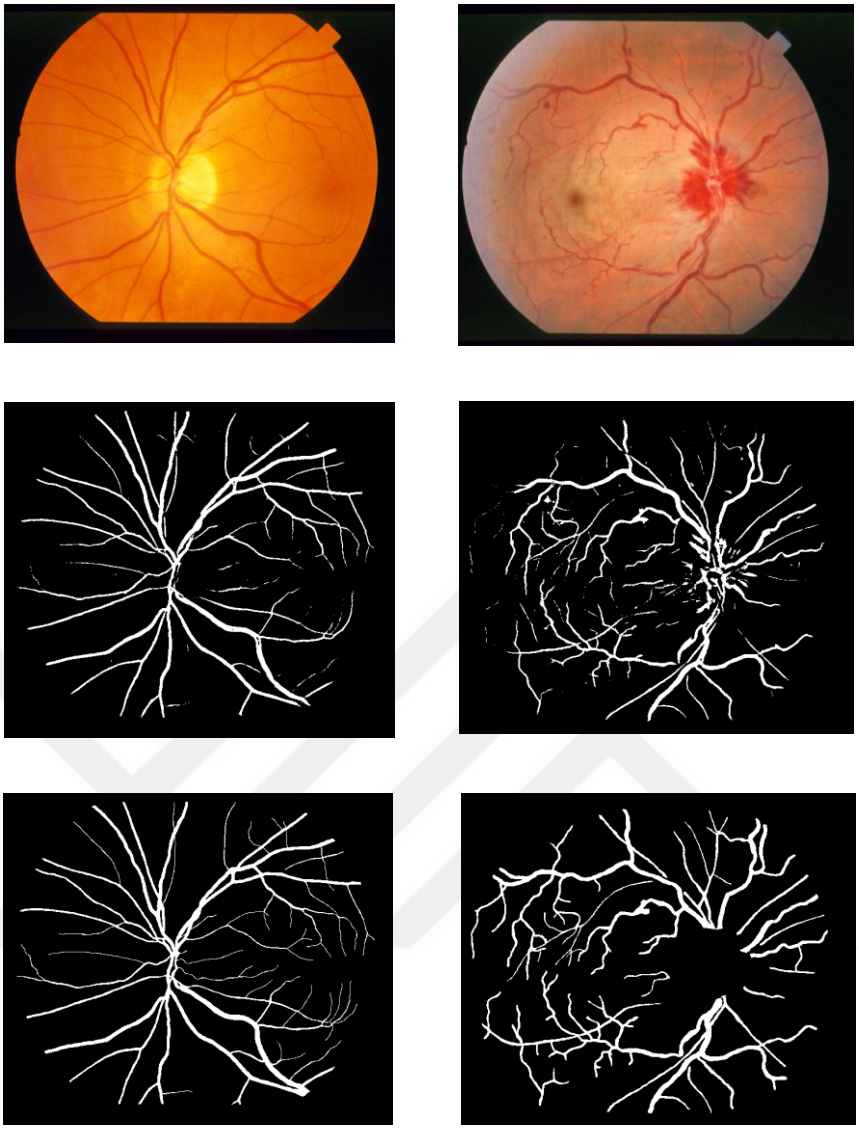

(a) (b)

Figure 3.12 Segmentation results for STARE database, first row: Input images, second row: segmentation results, third row: first human observer. a) best case accuracy b) worst case accuracy.

With respect to Table 3.3, which illustrates average performance measures for both DRIVE and STARE database, the average value of accuracy and precision rates incurred by the proposed method are higher than the second human observer in both databases. The average value of specificity for our algorithm are also higher than the second human observer for both databases which means that in the proposed method, few numbers of pixels that belong to the background or pathological regions are identified as part of a vessel than the second human observer. The average values of

area under ROC curve for both DRIVE and STARE database are 0.9682 and 0.9789 as illustrated in Figure 3.13.

Table 3.3 Performance measures on DRIVE and STARE database.

Database	Segmentation	SN	SP	ACC	AUC
DRIVE	2nd Human Observer	0.7796	0.9717	0.9464	_
	Proposed Method	**0.7545**	**0.9801**	**0.9513**	**0.9682**
STARE	2nd Human Observer	0.8955	0.9382	0.9347	–
	Proposed Method	**0.7556**	**0.9837**	**0.9605**	**0.9789**

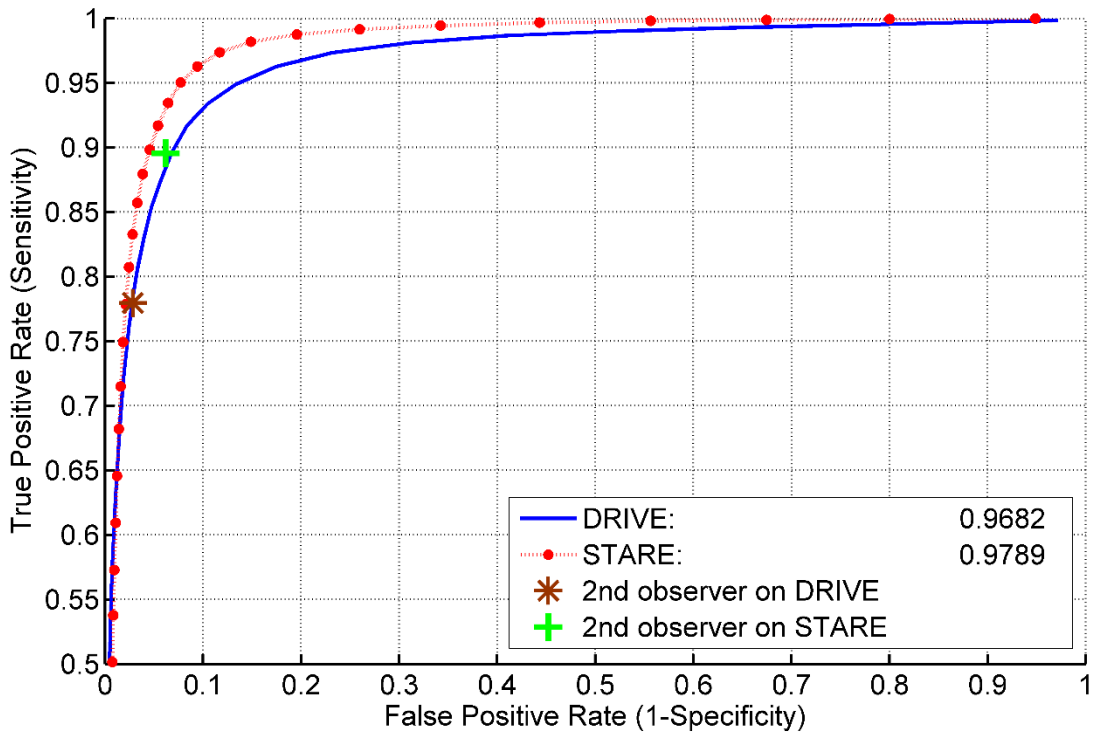

Figure 3.13 ROC curves for DRIVE and STARE database.

As can be seen in Figure 3.13, the ROC curves indicate that the performance of proposed method on DRIVE and STARE database is better than the second human observers.

3.4.3 Cross Training Result

For measuring the robustness of the proposed method for the training set, the cross-training method was used in such a way that the classifier trained on STARE (or DRIVE) database images is tested on DRIVE (or STARE) database images. The performance metrics for cross-training method were measured and Table 3.4 illustrates the value of these metrics. As can be seen, there is a small decrease for all of the metrics in both dataset in comparison to the Table 3.3, for instance, the value of accuracy is decreased from 0.9513 to 0.9496 for DRIVE database since the images in STARE database are different from DRIVE database.

Table 3.4 Cross-training result on DRIVE and STARE database.

Dataset	SN	SP	ACC	AUC
DRIVE (Trained on STARE)	0.7308	0.9740	0.9496	0.9595
STARE (Trained on DRIVE)	0.7453	0.9760	0.9545	0.9719

3.4.4 Comparison to Other Methods

For comparing the performance result of our method with other state-of-the-art methods, some metrics such as sensitivity, specificity, accuracy and area under ROC curve were used for evaluating this comparison. Tables 3.5 and 3.6 illustrates the value of the metrics for both DRIVE and STARE databases regarding the state-of-the-art algorithms published previously.

Table 3.5 Performance comparison of vessel segmentation methods on DRIVE database.

No	Type	Method	SN	SP	ACC	AUC
1.		2nd Human Observer	0.7796	0.9717	0.9470	_
2.	Unsupervised Methods	Zana (2001)	0.6971	N.A	0.9377	0.8984
3.		Jiang (2003)	N.A	N.A	0.9212	0.9114
4.		Mendonca (2006)	0.7344	0.9764	0.9452	N.A
5.		Al-Diri (2009)	0.7282	0.9551	N.A	N.A
6.		Lam (2010)	N.A	N.A	0.9472	0.9614
7.		Miri (2011)	0.7352	0.9795	0.9458	N.A
8.		Fraz (2012)	0.7152	0.9759	0.9430	N.A
9.		You (2011)	0.7410	0.9751	0.9434	N.A
10.		Azzopardi (2015)	0.7656	0.9704	0.9442	0.9614
11.	Supervised Methods	Niemeijer (2004)	N.A	N.A	0.9416	0.9294
12.		Soares (2006)	0.7332	0.9782	0.9461	0.9614
13.		Staal (2004)	N.A	N.A	0.9441	0.9520
14.		Ricci (2007)	N.A	N.A	0.9559	0.9558
15.		Lupascu (2010)	0.7200	N.A	0.9597	0.9561
16.		Marin (2011)	0.7067	0.9801	0.9452	0.9588
17.		Fraz (2012)	0.7406	0.9807	0.9480	0.9747
18.		Cheng (2014)	0.7252	0.9798	0.9474	0.9648
19.		**Proposed Method**	**0.7545**	**0.9801**	**0.9513**	**0.9682**

Table 3.6 Performance comparison of vessel segmentation methods on STARE database.

No	Type	Method	SN	SP	ACC	AUC
1.		2nd Human Observer	0.8951	0.9384	0.9348	_
2.	Unsupervised Methods	Hoover (2000)	0.6747	0.9565	0.9264	N.A
3.		Jiang (2003)	N.A	N.A	0.9009	N.A
4.		Mendonca (2006)	0.6996	0.9730	0.9440	N.A
5.		Al-Diri (2009)	0.7521	0.9681	N.A	N.A
6.		Lam (2010)	N.A	N.A	0.9567	0.9739
7.		Fraz (2012)	0.7311	0.9680	0.9442	N.A
8.		You (2011)	0.7260	0.9756	0.9497	N.A
9.		Azzopardi (2015)	0.7716	0.9701	0.9497	0.9563
10.	Supervised Methods	Soares (2006)	0.7207	0.9747	0.9479	0.9671
11.		Staal (2004)	N.A	N.A	0.9516	0.9614
12.		Ricci (2007)	N.A	N.A	0.9584	0.9602
13.		Marin (2011)	0.6944	0.9819	0.9526	0.9769
14.		Fraz (2012)	0.7548	0.9763	0.9534	0.9768
15.		Cheng (2014)	0.7813	0.9843	0.9633	0.9844
16.		**Proposed Method**	**0.7556**	**0.9837**	**0.9605**	**0.9789**

As can be seen in both Tables 3.5 and 3.6, the value of metrics in the proposed method is better than the most of the other methods. According to the Table 3.6, it can be seen that the only method that has better results than the proposed method with regard to the value of accuracy and AUC is the Cheng et al. (2014) method. Cheng et al. (2014) used 6% of random samples of entire dataset for training its classifier in STARE database while we used only 1%. Moreover, the feature vector that is extracted for each pixel is 17 dimension in the proposed method while Cheng (2014) used 280 dimension feature vector. Despite the high dimensionality of Cheng et al. (2014) method, for proving the fact that our method has the better performance

than Cheng et al. (2014) method, we evaluate the performance of our method by using the 6% of entire samples in training stage just like Cheng et al. (2014) method. And we could achieve the value 0.9650 and 0.9855 for accuracy and AUC which shows that the proposed method has the higher performance than Cheng et al. (2014) method. Moreover, the leave one out method is also applied in the STARE database. As a result of this implementation, we could achieve the values of 0.9579 and 0.9772 for accuracy and AUC metrics which shows that our method has the better result than Soares et al. (2006) and Staal et al. (2004) method as can be seen in Table 3.6. Therefore, it can be claimed that the value of accuracy and area under ROC curve achieved by the proposed method has better results than all of the state-of-the-art methods in STARE database.

As the Table 3.7 illustrates, in the case of cross-training of classifier our method has the average value of accuracy higher than all of the other state-of-the-art methods in both DRIVE and STARE databases.

Table 3.7 Performance comparison of results with cross-training in terms of average accuracy.

Method	DRIVE(Trained on STARE)	STARE(Trained on DRIVE)
Soares (2006)	0.9397	0.9327
Ricci (2007)	0.9266	0.9464
Marin (2011)	0.9448	0.9528
Fraz (2012)	0.9456	0.9493
Cheng (2014)	0.9384	0.9476
Proposed Method	**0.9496**	**0.9545**

In order to compare the performance of proposed method on the pathological images, 10 images of STARE database that are pathological images, as described in section 2.2, were used for comparison. The average value of sensitivity, specificity and accuracy for 10 pathological images were computed. As can be seen in Table 3.8, the average value of accuracy by the proposed method has the highest value than

other methods which shows that our algorithm is robust in the case of segmentation of abnormal images.

Table 3.8 Performance comparison of results on pathological images (STARE database).

Method	SN	SP	ACC
2nd Human Observer	0.8719	0.9384	0.9324
Hoover (2000)	0.6587	0.9565	0.9258
Soares (2006)	0.7181	0.9765	0.9500
Fraz (2012)	0.7262	0.9764	0.9511
Proposed Method	**0.7017**	**0.9836**	**0.9573**

3.5 Summary

In chapter, we proposed an effective method for the segmentation of the retinal blood vessels based on supervised learning method. We constructed 17 dimensional feature vector consisting of CLAHE contrast enhancement feature, vesselness measurement, morphological transformation, multi-scale response of Gabor wavelet and also B-COSFIRE filter response which are used for the first time in supervised learning based methods. Random forest classifier which is very flexible for fusing the inharmonious features was utilized for classifying each pixel as vessel or nonvessel pixel.

The proposed method is tested on the two public online available database, DRIVE and STARE database. The performance of the proposed method was also compared against more than 15 other methods on STARE and DRIVE dataset respectively. The results shows that the performance of a proposed method is better than other state-of-arts methods with respect to the accuracy and area under ROC curve.

CHAPTER FOUR
WIDTH AND TORTUOSITY MEASUREMENT OF RETINAL VESSEL

4.1 Overview of Proposed Method

Extraction of retinal blood vessels gives a suitable opportunity to the analysis of the vascular system directly. There are several important abnormalities of the retinal related to the vascular system as described in first chapter, for instance, diameter changes in the retinal vessels according to entire vascular system are associated with the cardiovascular diseases, A/V ratio, and the unusual changes in diameter along a single vessel are also one of the important predictors of proliferate diabetic retinopathy. Moreover, identifying the thin blood vessels and the percentage of them with regarding the entire vasculature system is an important task for prediction the diabetic retinopathy diseases. Also, the tortuosity of retinal blood vessels has been associated with a number of established risk factors for cardiovascular outcomes. Thereby measuring the diameter and tortuosity of the retinal blood vessels, both arteries and veins, and analyzing the vessels according to the corresponding metrics gives significant information about pathology.

In this chapter, we establish an automatic system for measuring the diameter and tortuosity of the blood vessels in retinal fundus images and analyzing the vasculature system according to various metrics. The corresponding system includes the three main stages. In the first stage, the retinal blood vessels extracted using the method proposed in chapter 3. The following stage is a preprocessing stage which itself consists of four steps to prepare vessels for further processing. As the last stage, two important algorithms are utilized for measuring the diameter and tortuosity of retinal blood vessels. The schematic of the proposed method can be seen in Figure 4.1.

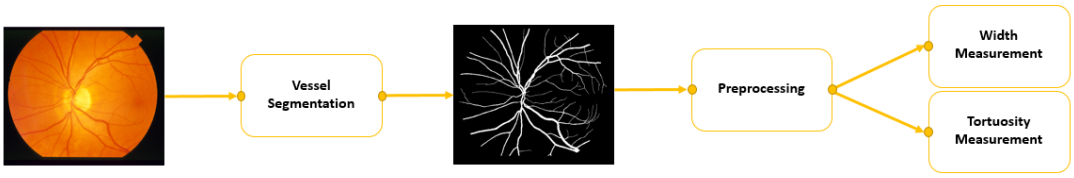

Figure 4.1 General framework of proposed automatic method for measuring the width and tortuosity of retinal blood vessels.

4.2 Retinal Vessel Width Measurement

In this section, first the methodology of the proposed method for automatic width measurement of retinal blood vessels is introduced in the first subsection and different analysis based on the diameter of retinal blood vessels is presented in the next subsection.

4.2.1 The Methodology

For measuring the diameter of retinal blood vessels, an initial vessel segmentation stage is needed to extract the vessel segment profiles. The method proposed in chapter 3 is utilized to extract retinal blood vessels tree. It is important to be noticed that all the parameters in the feature extraction stage and classification stage in the corresponding vessel extraction method are the same as referred previously. As it was mentioned in section 3.4.1, the output of classifier is a vessel probability map. A simple threshold must be applied to the probability map for achieving the vessel segments. The smaller you choose the value of threshold, the more vessels will be extracted. Therefore, small threshold value is selected in compare to the section 3.4, in order to extract more thin blood vessels.

With regard to the fact that the diameter measurement algorithm is based on the vessel center line, after achieving the vessel network in the previous stage, a preprocessing algorithm includes four steps is applied to the binary image of vessel network to extract the vessels center lines and make the corresponding network

reliable for further processing. In the first step, all of the connected components, eight connectivity, in the vessel network are identified. It means that the connectivity between the vessel pixels is identified and the small connected components are then emitted from vessel network for removing the small false detected regions and the very small and short blood vessels created in the vessel extraction stage. With regard to the fact that the method utilized for width measuring is based on the centerline of the vessels, in the second step, a simple thinning method called morphological sequential thinning operation (Lam et al., 1992) is applied to the binary image for achieving the centerline of blood vessels. This operation results in one pixel wide connected skeletons and piecewise linear skeleton of blood vessels. In the next step, all of the crossing and bifurcation points in the vessel centerline image are identified by a simple definition of connectivity of centerline pixels and they are removed for extracting the vessel centerline fragments. A bifurcation point is defined as a centerline pixel with three or more connected neighbors. As the last step, the corresponding vessel centerline fragments image is scanned with regarding the connectivity of each centerline pixels for finding the end points of each centerline fragments. An end point is defined as a centerline pixel with only one connected neighbor. After finding both end points of each fragment in vessel centerline, the corresponding points is deleted and this action is repeated for five or six times in order to prevent the interface of the endpoints of different fragments in the further processing, width measurement. The fragmented vessel centerlines obtained from this algorithm are illustrated in Figure 4.2.

After achieving the vessel centerline fragments image in the preprocessing stage, one of most popular method introduced by Nguyen et al. (2013) is utilized for measuring the diameter of retinal blood vessels. According to the literature, there are several methods for measuring the diameter of blood vessels in retinal fundus images. In this work, Nguyen et al. (2013) method is used since this algorithm is very simple and more precise than other methods with regarding the results in the corresponding paper. The proposed method by Nguyen et al. (2013) is based on the vessel edges and vessel centerline in such a way that a pair of edge points is identified at a specific center point that the distance between the corresponding edge

points represents the vessel width with regarding the specific center point. The simple algorithm is introduced for extracting the edge image of vessels. After extracting the vessel network in the first stage, the corresponding image is scanned with regarding the connectivity of each vessel pixels for finding the edge pixels of vessels. An edge point is defined as a vessel pixel with at least one non vessel pixel in eight neighborhood. Figure 4.3 illustrates an example of edge detection.

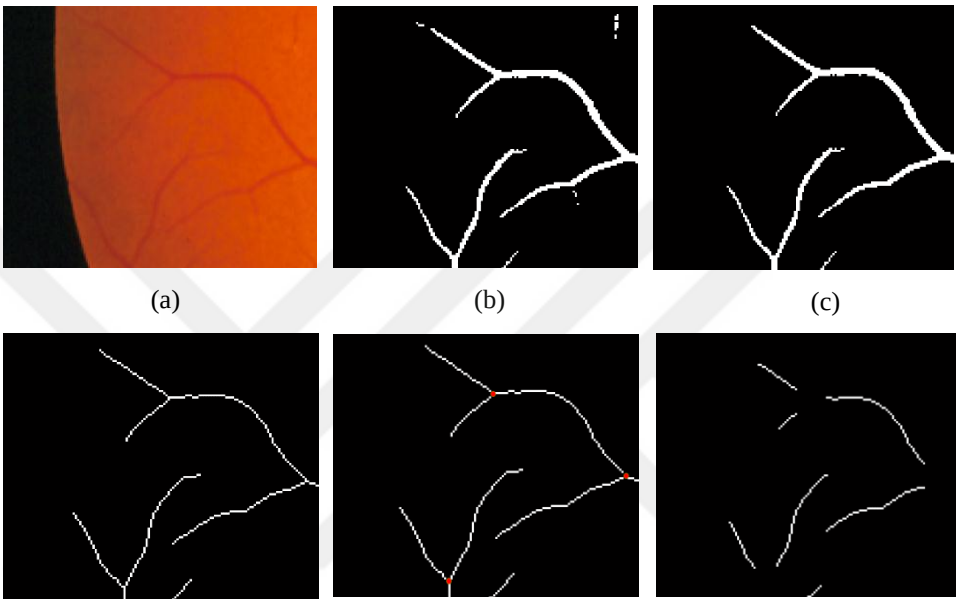

Figure 4.2 Fragmented vessel centerlines obtained in preprocessing stage. a) cropped region from original RGB image b) vessel network tree extracted by proposed method in chapter 3 c) removing small connected component d) the result of applying the thinning algorithm e) identifying the crossing and bifurcation points specified by red points and deleting them f) identifying the end points in each segment and deleting them iteratively.

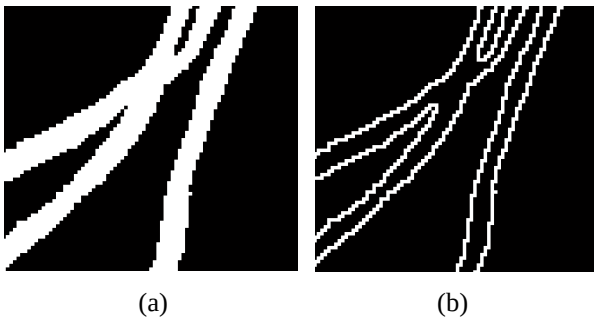

Figure 4.3 Vessel edge detection. a) vessel image after extrction process b) edge image after applying edge detection algorithm.

With regarding the vessel centerline fragments image and the vessel edge image, the Nguyen et al. (2013) algorithm is designed in such a way that at each center point, all edge points (points in edge image) that are within a certain mask centered on the corresponding center point are determined. After that, for each edge point, its mirror point located in the other edge side and forms 180^0 angle with current edge point is identified. In order to detect the correct mirror point for all the edge points, the angle a_i is defined for each edge point E_i by the vector pointing from the center point to the corresponding edge point and the vector representing the horizontal line is computed. Thereby, an edge point E_j is defined as the mirror point of E_i if:

$$-\varepsilon < \left|a_i - a_j\right| - 180 < \varepsilon \tag{4.1}$$

Where ε is the difference between the angle formed by two edge points and the difference in the ideal case, 180^0, which is set to 5^0 as referred by Nguyen (2013). After identifying the pairs of edge points around the corresponding center point, the edge points with the shortest length is defined as the goal edge points that the distance between these points represents the vessel width at the corresponding center point. This algorithm repeated for all of the center points along a vessel and the average value of corresponding widths represents the diameter of the vessel. The schematic of the algorithm can be seen in Figure 4.4.

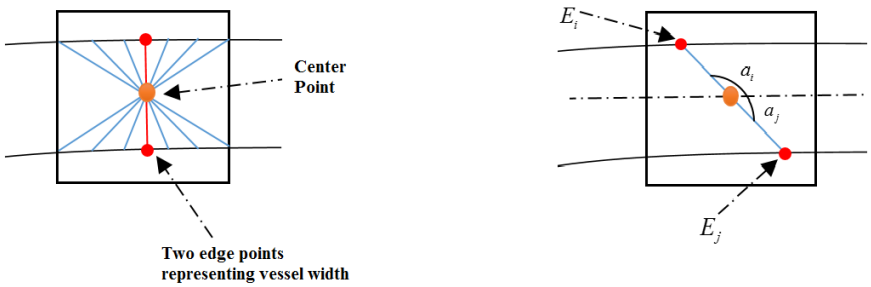

Figure 4.4 algorithm for deretmining the vessel ege points representing vessel width at a specific center point.

The width of each fragmented vessel can be calculated by below formula,

$$W_i = \frac{1}{N_i} \sum_{j=1}^{N} W_j \tag{4.2}$$

Where W_i is the average width value of *i*-th vessel, N_i is the totall number of center points along ith vessel and W_j is the width of vessel with respect to the jth center point.

4.2.2 Retinal Vessel Width Analysis

In this subsection, the results of width measurement algorithm are analyzed with regard to the some parameters. There are three important outputs of width measurement algorithm applied to the retinal fundus image such as the number of center points along each fragmented vessel (N), width (W) and standard deviation (σ) of each fragmented vessel with regarding the widths of all center points along the corresponding fragmented vessel. The value of width can be measured using the Equation (4.2) for each fragmented vessel and the standard deviation also can be calculated by below formula also,

$$\sigma_i = \sqrt{\frac{1}{N_i} \sum_{j=1}^{N} \left(W_j - W_i \right)^2} \tag{4.3}$$

The images of STARE database without any pathologies are utilized for analyzing. The example of the output of width measurement algorithm for one of these images can be seen in Table 4.1.

Table 4.1 Output of the width measurement algorithm for image 0120 from STARE database.

Number of Vessel	Number of center points (N)	Width (W)	Standard deviation (σ)
1	23	1	0
2	9	1	0
⋮	⋮	⋮	⋮
33	88	2.3	0.20
⋮	⋮	⋮	⋮
88	110	3.35	0.46
110	10	1.6	0.01
111	98	2.62	0.02
⋮	⋮	⋮	⋮
139	19	1	0

As can be seen in above table, there are four columns which the first column refers the number of the fragmented vessel, the second one is the total number of center points located along the corresponding fragmented vessel, the third column indicates the width value of the corresponding vessel and the last column is the standard deviation.

With respect to the results of the width measurement algorithm, the histogram analysis is done for determining the percentage of the thin vessels in the entire vessel network with regarding the vessel widths. The image 0120 from STARE database is used for this analysis. As a first step, the corresponding width measurement algorithm is applied to the image. Table 4.1 is the result of this application. After achieving the results, the histogram of the vessels width is plotted with regard to the number of vessels and the diameter of the vessels. Figure 4.5 illustrates the histogram of vessels width.

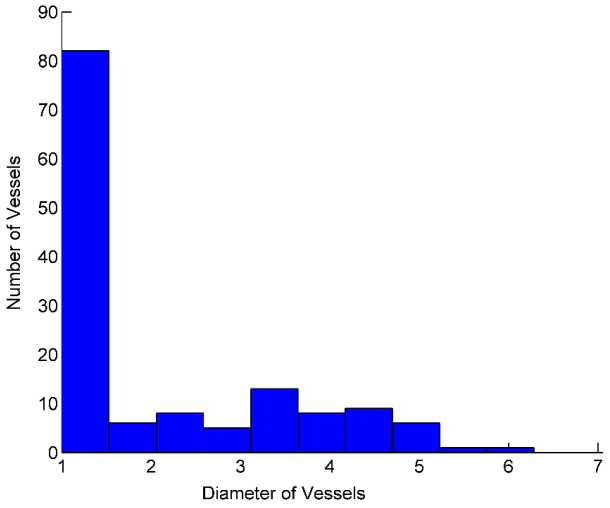

Figure 4.5 Histogram of vessels width related to the image 0120 from STARE database.

As can be seen in Figure 4.5, the number of thin vessels is more than thick vessels. As it was referred in section 1.2, identifying the thin blood vessels and the percentage of them with regarding the entire vasculature system is an important task for prediction the diabetic retinopathy diseases. Therefore, it is very easy to calculate the percentage of the thin vessels using the corresponding histogram. For instance, in Figure 4.4, a total number of the vessels is 139 and a total number of the thin vessels with diameter value of 1 or lower is 82, so by this way the corresponding percentage can be calculated easily. Another important application of this histogram is that if there are two different histograms related to the two different fundus images captured in different period of times from the same patient, it is very easy to determine the presence of new thin blood vessel by comparing the corresponding two histograms which refers the presence of diabetic retinopathy diseases also.

Standard deviation is another parameter that gives the meaningful information about the presence of diabetic retinopathy and plus diseases introduced in section 1.2. Normal fragmented blood vessel should has the constant value of width along the different center points of corresponding vessel, but sometimes the diameter of blood vessel alters along the center points of the vessel because of the presence of several diseases. According to the fact that our width measurement method is based on the mean value of the widths of individual center points along vessel, it is also

possible to measure the standard deviation of widths along the vessel using Equation (4.3). The important point that should be noticed is that vessel that has no diameter changes along center points must have the zero or low value of standard deviation with respect to the Equation (4.3). On the other hand, the vessel that has diameter changes along center points should have high value of standard deviation. Thereby, the corresponding parameter is very important factor for determining the abnormalities in vessels. Some of these abnormalities can be seen in Figure 4.6.

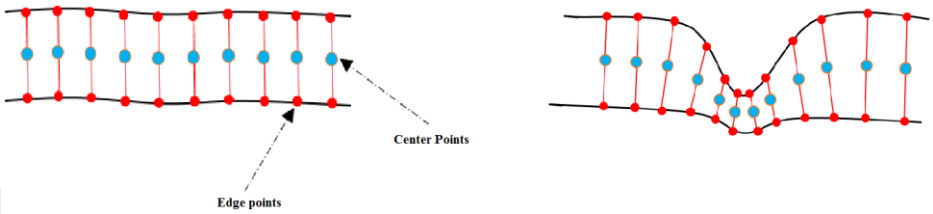

Figure 4.6 Diameter changes along the vessel. Left one is a normal vessel with low or zero value of standard deviation. Right one is an abnormal vessel with high value of standard deviation.

For analyzing the standard deviation values of vessels in image 0120 of STARE database, the histogram of corresponding vessel with regarding the values of standard deviation is plotted. The result of the histogram is illustrated in Figure 4.7. As can be seen, the values of the standard deviation for all of the vessels are low which means that there is no abnormalities related to the vessels width changes.

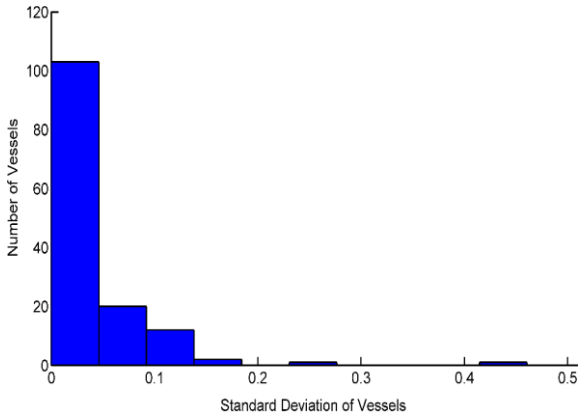

Figure 4.7 Histogram of the vessels with regarding the value of standard deviation.

Moreover, if the detail of the fragmented vessels is available, it means that all of the vessels can be separated into two groups as arteries and veins, one of the most important metrics that is called A/V ratio can be calculated easily. It should be referred that the changes in the ratio between the diameter of retinal arteries and veins, also called A/V ratio, is specified in the case of hypertension and atherosclerosis.

4.3 Retinal Vessel Tortuosity Measurement

As a first step, the methodology of the proposed algorithm for automatic tortuosity measurement of retinal blood vessels is described and in the following step, different images are analyzed by applying the proposed method on corresponding images.

4.3.1 The Methodology

The proposed method for automatic measurement of the retinal blood vessels tortuosity include three main stages, vessel segmentation stage, preprocessing stage and tortuosity measurement stage.

For measuring the tortuosity of the retinal blood vessels, an initial vessel segmentation stage is needed to extract the vessel segment profiles. The method proposed in chapter 3 is utilized to extract retinal blood vessels tree. It is important to be noticed that all the parameters in the feature extraction stage and classification stage in the corresponding vessel extraction method are the same as referred previously.

According to the fact that the tortuosity measurement algorithm is based on the vessel centerline, after achieving the vessel network in the previous stage, a preprocessing algorithm described in the subsection 4.2.1 is utilized for achieving the vessel centerline network. The only difference here is that the end points are not deleted in the last step of the preprocessing stage. It means that the tortuosity

measurement algorithm is applied on the fragmented vessels without deleting the end points of the corresponding vessels. The result of applying vessel segmentation algorithm and preprocessing technique can be seen in Figure 4.2.

After achieving the vessel centerline fragments image in the preprocessing stage, one of the most popular methods, known as Slop Chain Code (SCC), introduced by Bribiesca (2013) is utilized for measuring the tortuosity of the retinal blood vessels. According to the literature, there are several methods for measuring the tortuosity of the blood vessels in the retinal fundus images. Due to the several advantages, the SCC algorithm is constructed for measuring the tortuosity of the retinal blood vessels. The most important advantages of the SCC is that the corresponding algorithm is very simple, independent of translation, rotation and optionally of scaling and more precise than other methods with regarding the results in the corresponding paper.

If we define a vessel centerline as a curve, The SCC of a curve is achieved by placing straight lines segments of constant length around the curve and measuring the slope changes between contiguous straight line segments scaled to a continuous range from -1 to 1. The slope changes scaled to lie within (-1, 1) can be seen in Figure 4.8.

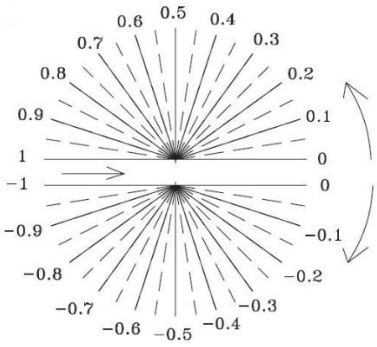

Figure 4.8 Range of slope changes (Bribiesca, 2013).

With regard to the fact that a fragmented vessel centerline is a continuous curve, to convert a continuous curve into a discrete curve the length of the straight line segments is selected for describing such a curve. After fixing the length of the

straight line segment, a point of a curve is selected as an origin point or start point and an endpoint of one of the straight line segments is set to coincide with this origin. The opposite endpoint is set over the corresponding curve, determining the starting point of next segment, and so on. With regard to the graphically description, this process achieves to superimposing the sequence of circles traveling around curve that the intersections of the circles determine the points of the discrete shape and the radius of each circle represents the length of the segment as can be seen in Figure 4.9

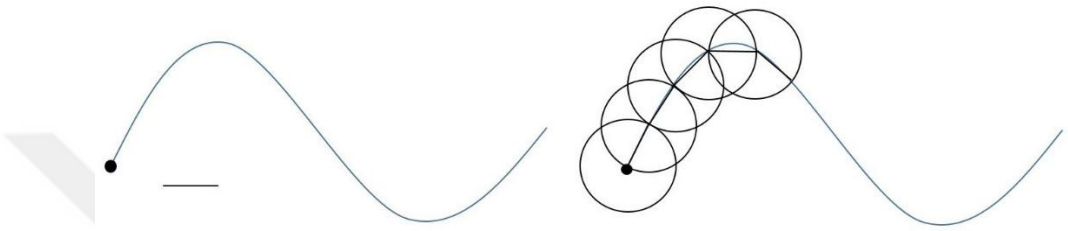

Figure 4.9 Conversion of a continuous curve into a discrete curve. The left shape: a continuous curve with a selected origin and a straight line segment. The right shape: traversing the curve using circles to determine slope changes.

A chain a is defined as an ordered sequence of n elements that can be represented by,

$$a = a_1 a_2 \ .... \ a_n = \{a_i : 1 \le i \le n\} \tag{4.4}$$

The sequence of slope changes is the chain that defines the discrete shape of the continuous curve. Therefore, the chain code of the curve shown in Figure 4.10 is as follows: -0.05 -0.04 -0.27 -0.20 -0.10 0 0 0.05 0.12 0.023 0.1 0 0.05. The important point that should be noticed is that the number of straight line segments is equal to the number of slope changes plus one.

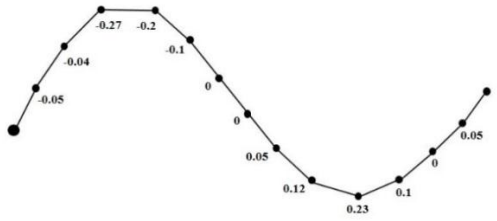

Figure 4.10 Discrete curve and its ordered sequence of slope changes.

The length (L) of each straight line segment is equal to the perimeter of the curve (P) divided by the number of the straight line segments (m), i.e., L=P/m. For instance, in Figure 4.10, m=14 is selected and P=15.30, therefore, L=1.09. The tortuosity of a curve represented by a chain is the sum of all absolute values of the chain elements as can be seen in below formula,

$$\tau = \sum_{i=1}^{n} |a_i| \tag{4.5}$$

For any curve the minimum and maximum values of tortuosity belong to the range $[0, n)$. For instance, in the Figure 4.10, the tortuosity value of the corresponding curve is 1.11 as follows,

$$\tau = |a_1| + |a_2| + ... + |a_{13}| = 0.05 + 0.04 + ... + 0.05 = 1.11 \tag{4.6}$$

There are some important properties about the SCC of a curve that should be referred. One of these important points is that the inverse of a chain of a curve is another chain with opposite sign elements of the first chain in inverse order. It means that changing the start point in the curve for obtaining a chain of the slope changes does not change the tortuosity value as can be seen in Figure 4.11.

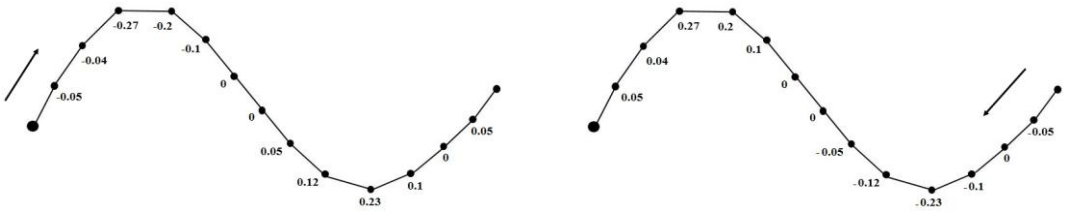

Figure 4.11 the inverse of a chain. The left curve: the curve and its chain. The right curve: the inverse of the chain. As can be seen, both curve have the same tortuosity value (1.11).

4.3.2 Retinal Vessel Tortuosiy Analysis

In this subsection, the results of tortuosity measurement algorithm are analyzed with regard to the some parameters. There are two important outputs of tortuosity

measurement algorithm applied to the retinal fundus image includes the length of the fragmented vessels (L) and the tortuosity (τ) of the corresponding fragmented vessels. The perimeter of a fragmented vessel can be measured by summation of the distances between each pixel along the vessel. The important point that should be referred is that the Euclidean distance is utilized for measuring the distance between centerline pixels. Also, the value of tortuosity for each fragmented vessel can be measured using Equation (4.5). Moreover, the width of each fragmented vessel is calculated in order to further analysis using Equation (4.2).

Eight images of STARE database are utilized for analyzing, four images with vessel tortuosity and four images without any pathologies. The example of the output of tortuosity measurement algorithm for the image 0199 from STARE database can be seen in Table 4.2.

Table 4.2 Output of the tortuosity measurement algorithm for image 0199 from STARE database.

Number of Vessel	**Length (L)**	**Tortuosity (τ)**	**Width (W)**
1	160.19	1.07	1
2	81.87	0.88	3.07
⋮	⋮	⋮	⋮
	56.11	1.48	2.66
⋮	⋮	⋮	⋮
47	40.04	1.52	1.45
48	104.66	1.74	1.50
49	124.95	3.92	1.46
⋮	⋮	⋮	⋮
109	59.87	1.81	3.04

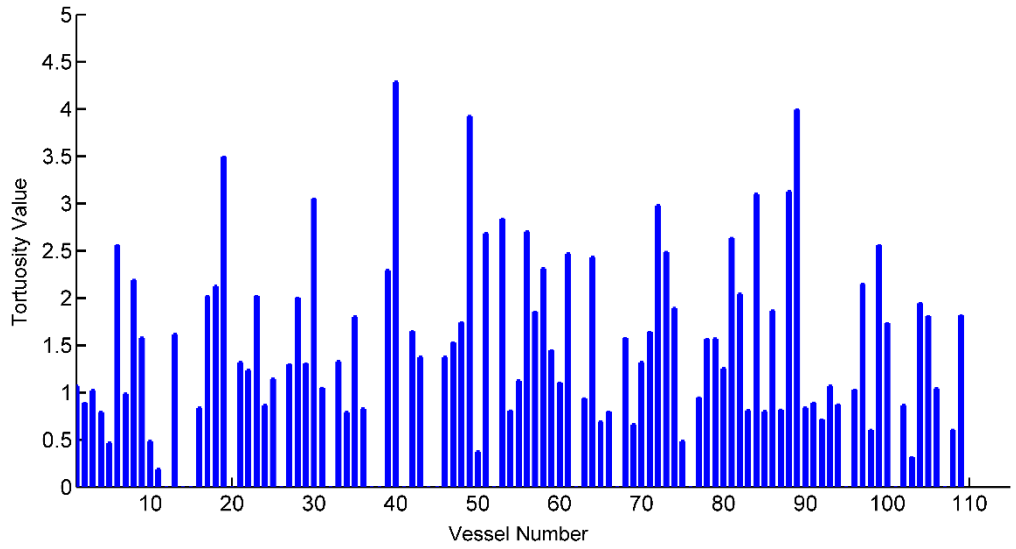

Figure 4.12 Tortuosity value of the fragmented vessels in the image 0018 from STARE database.

As can be seen in above table, there are four columns which the first column refers the number of the fragmented vessel, the second one is the length of the corresponding fragmented vessel, the third and fourth columns indicates the tortuosity and width value of the corresponding vessel. Figure 4.12 illustrates the tortuosity value of the different vessels with regard to the Table 4.2. The fundus retinal image 0018 from STARE database also can be seen in Figure 4.14.

With regard to the results of the tortuosity measurement algorithm, the histogram analysis is done for determining the percentage of the tortuous vessels in the entire vessel network. The image 0199 from STARE database is used for this analysis. As a first step, the corresponding tortuosity measurement algorithm is applied to the image 0199. Table 4.1 and Figure 4.12 are the results of this application. After achieving the results, the histogram of the vessels tortuosity is plotted with regard to the number of vessels. Figure 4.13 illustrates the histogram of vessels tortuosity.

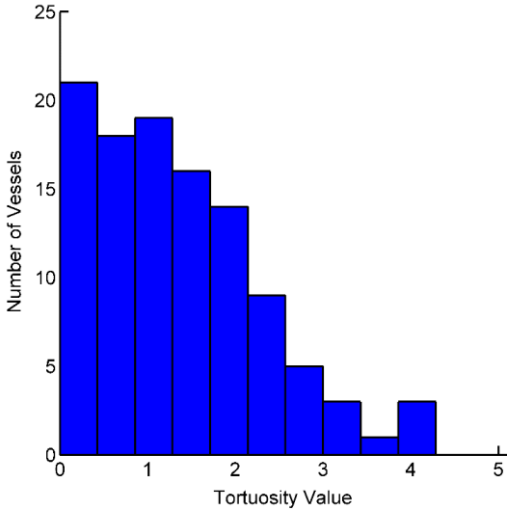

Figure 4.13 Histogram of vessels tortuosity related to the image 0199 from STARE database.

As can be seen in Figure 4.13 the percentage of the vessels with the high value of tortuosity can be measured by an expert. For instance, if the tortuosity value of a vessel can be classified in three classes by an expert includes normal vessel, low tortuous vessel, and high tortuous vessel, the percentage of each class can be measured easily from the above histogram. Moreover, if there are two different histograms related to the two different fundus images captured in the different period of times from the same patient, it is very easy to determine the presence of tortuous vessel by comparing the corresponding two histograms which refers the presence of plus diseases also.

For achieving the single value of the tortuosity of the entire vessel network, the mean value of the tortuosity of individual fragmented vessels measured using below formula,

$$\tau_m = \frac{\sum_{i=1}^{N} \tau_i}{N} \tag{4.7}$$

Where N is the total number of vessels in the entire network. The goal of measuring the corresponding parameter is that the tortuosity value of the entire vessel network in different images can be easily compared using single value for

determining the pathologies like plus diseases. The value of τ_m is 1.32 for image 0199 from STARE database shown in Figure 4.14.

For comparing the above parameter in different images, the small subset includes eight images of STARE database are utilized. The corresponding images can be seen in Figure 4.14. Four number of images are normal image without any pathologies and four of them are images with tortuous vessels. The corresponding algorithm for tortuosity measurement is applied to the images and the value of τ_m is measured for all images. The result of the corresponding measurement is illustrated in Table 4.3

Table 4.3 Vessel tortuosity based on the entire image area in tortuous and non tortuous images.

No.	**Non tortuous**		**Tortuous**	
	Image	Tortuosity(τ_m)	Image	Tortuosity(τ_m)
1	0120	0.6538	0018	1.0784
2	0162	0.7403	0027	1.0689
3	0163	0.7344	0217	1.0977
4	0255	0.7067	0199	1.3165

As can be seen in above table, the corresponding values of tortuosity in the images with tortuous vessels are higher than the images with non tortuous vessels which indicates that the corresponding parameter of tortuosity is a reliable parameter for comparing or classifying the images as tortuous or non tortuous images. The classification approach can be done by specifying the constant value of tortuosity as a threshold value by an expert. Moreover, after separating the corresponding images as a tortuous or non tortuous images, the images placed in the tortuous group also can be classified in the different levels with regarding the value of tortuosity as low tortuous, normal tortuous and high tortuous levels.

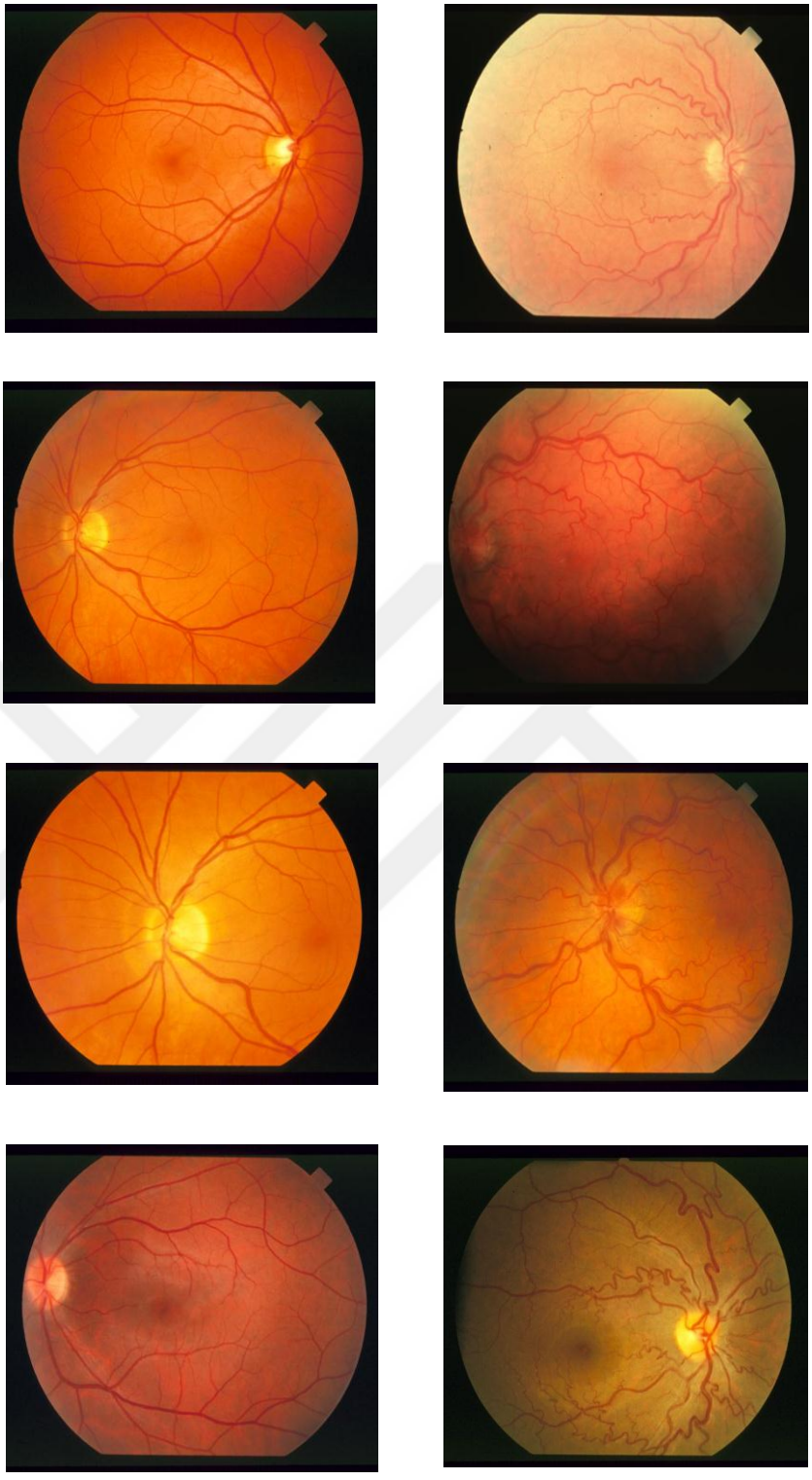

(a) (b)

Figure 4.14 Small subset of images of STARE database includes eight images. a) images without any pathologies, from up to bottom, image 0120, 0162, 0163 and 0255 b) images with tortuous vessels, from up to bottom: image 0018, 0027, 0217 and 0199.

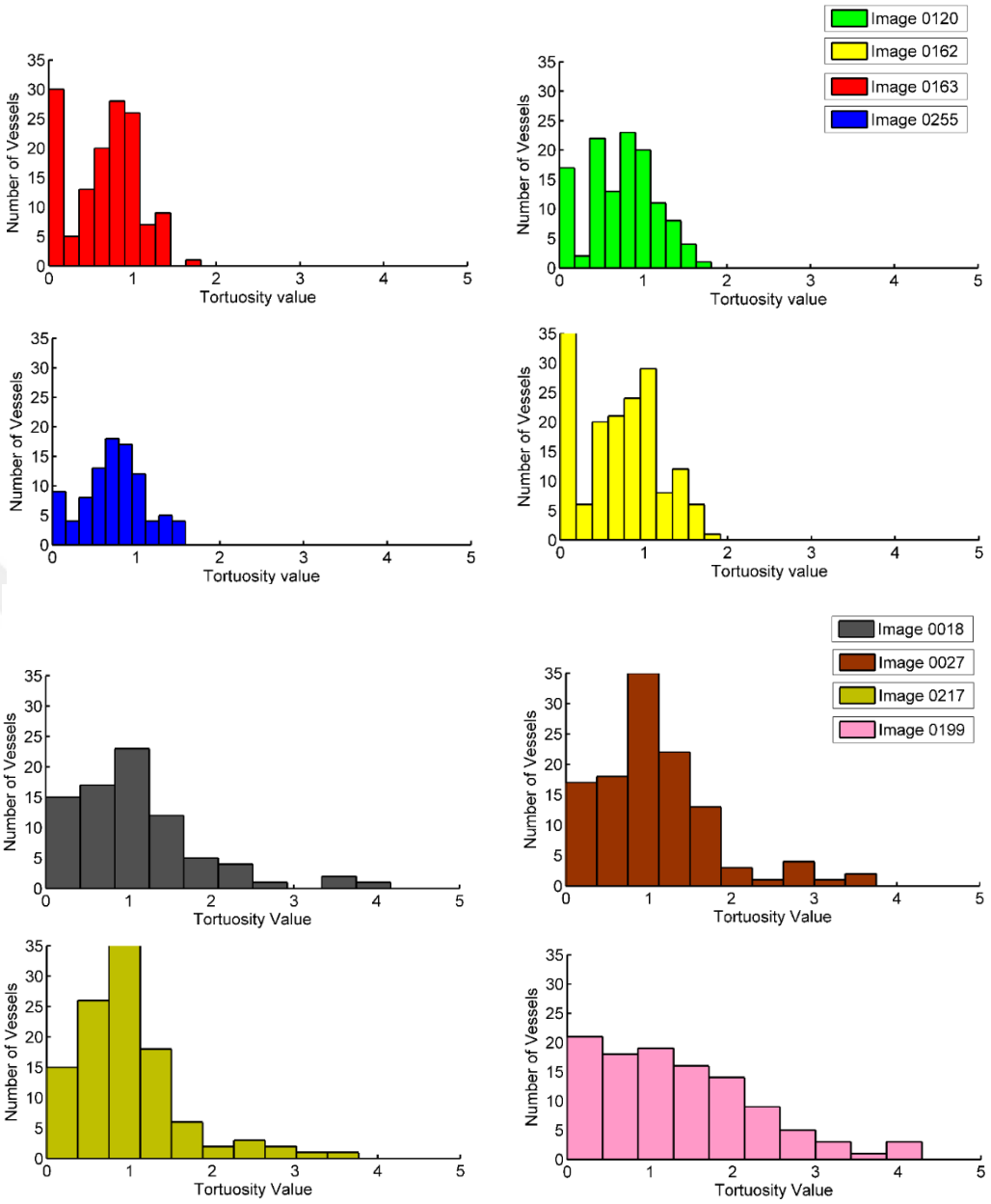

Figure 4.15 Vessel tortuosity histogram of images 0120, 0162, 0163, 0255, 0018, 0027, 0217 0199 from STARE database.

The histogram of vessel tortuosity for all of the images also is plotted in order to compare the tortuosity value of vessels in different images. The result of this application is shown in Figure 14.15.

With respect to the corresponding histograms in the Figure 4.15, all of the images categorized as normal images without any pathologies have a compacted or

centralized distribution of vessel tortuosity in such a way that the range of tortuosity for all of the vessels alters from 0 to 1.8. Therefore, as can be seen in the histogram of normal images the bars gathered in the left side of the graph.

In contrast to the histogram of the normal images, the distribution of the vessels with regard to the value of tortuosity in the images with tortuous vessels is more spread. As can be seen in the histogram of images with tortuous vessels the range of tortuosity alters from 0 to 4.5 which indicates the presence of specific diseases.

The important point that should be noticed is that for specifying the image as a pathologies image with regard to the corresponding value of tortuosity in the histogram, the constant value of tortuosity must be determined as a threshold value by an expert. It means that the image that has vessels with tortuosity values more than the threshold value is specified as a pathology image.

4.4 Summary

In this chapter, an automatic system was developed for analyzing the vasculature system by measuring the diameter and tortuosity of the retinal blood vessels. The corresponding system includes three main stages, vessel extraction, preprocessing, and vessel properties measurements. The hybrid feature vector and ensemble classifier was utilized for extracting the network of blood vessels. In the following step, a preprocessing algorithm is introduced for preparing the correspond network for further analysis. In the last stage, the two important algorithms based on the edges and centerline of fragmented vessels were utilized for measuring and analyzing the diameter and tortuosity of blood vessels.

Different kind of analysis was done based on the histograms of vessels with regard to diameter and tortuosity values for identifying the abnormal structures in the retinal images. Moreover, several parameters such as the means value of tortuosity and standard deviation of vessel width were introduced in order to compare different images with normal and abnormal blood vessels.

CHAPTER FIVE
DISCUSSION AND CONCLUSION

The aim of this thesis is to develop an automatic computer system for diagnosis of several diseases by analyzing the retinal fundus images. As a first step, we proposed a robust and reliable method for retinal blood vessel segmentation based on the pixel feature classification algorithm. The strong experimental results are achieved by testing the proposed method on different databases and comparing the corresponding results with existing methods in the literature. The results have shown that our method is robust and efficient in the segmentation of retinal blood vessel compare to the other methods. In the next step, we developed an automatic system for measuring the two important properties of extracted vessels, diameter and tortuosity, in order to analysis the vasculature system according to the various parameters. The results shows that the corresponding parameters are reliable and powerful for detecting abnormalities in the different images.

5.1 Blood Vessel Segmentation

In this thesis, we provide the novel method for retinal blood vessel segmentation. The proposed method is based on the classification algorithm known as pixel feature classification. We constructed 17 dimensional feature vector consisting of CLAHE contrast enhancement feature, vesselness measurement, morphological transformation, multi-scale response of Gabor wavelet and also B-COSFIRE filter response which are used for the first time in supervised learning based methods. Random forest classifier which is very flexible for fusing the inharmonious features was utilized for classifying each pixel as vessel or nonvessel pixel. The classifier was trained by selecting the 300,000 samples randomly from DRIVE database and 60,000 sample from STARE database. Despite that number of samples which are used for training stage on STARE database for the proposed method are less than other multi-feature supervised methods, Soares et al. (2006), Fraz et al. (2012) and Cheng et al. (2014) in order used 1 million, 200,000 and 75,000 samples, the average value of

accuracy (0.9606) and area under ROC curve (0.9789) for our method are higher than all of the state-of-the-art methods.

With regarding the cross training results, the proposed method has the highest value of average accuracy in both DRIVE (0.9496) and STARE (0.9545) databases compared to other methods which show that the proposed method is very robust to training set used while other methods are more dependent on the training set. This training set robustness allows our algorithm to be used on multiple datasets without retraining, which is very useful for large-scale screening programs.

Moreover, the performance of the proposed method on the pathological images is better than other state-of-the-art methods. The average value of accuracy in proposed method for 10 abnormal images from STARE database is 0.9573 which is the highest value among other methods. This result shows that our method is very robust for segmentation of abnormal images.

In order to achieve the better result of segmentation, more than 10 classifiers also is used in the classification stage instead of the RF classifier such as support vector machine (SVM), multi-layer perceptron (MLP), bayesian classifier, adaboost, bagging and boosting and random subspace (RS). The important point that should be noticed about the result of the corresponding implementation is that the performance of the RF classifier is better than all of the other classifiers. Moreover, different kind of features of each pixel also is extracted in order to increase the performance of RF classifier. These features include line strength (Ricci et al., 2007), weber local description (WLD) (Cheng et al., 2014), local binary pattern feature (LBP) and e.t. But according to the fact that these features have not effected to the performance of the classifier, we refused to use them.

As described previously, one of the disadvantages of supervised learning methods for vessel segmentation is that they are time-consuming. Among other state-of-the-art methods, our method is not an exception. In this work, the time required for segmenting an input image is built of two parts: feature extraction and random forest

classifier. The first part is composed of extracting five different kinds of features. For random forest classifier, the calculation time depends on the number of the decision trees (150 is selected) and the value of depth for each decision tree (15 is selected). In both DRIVE and STARE database images, the average time for segmenting an image including feature extraction and classification is around 120 seconds. We have used MATLAB for implementing all experiments on an Intel(R) Core(TM) i7 CPU (1.73GHz) with 8GB memory.

5.2 Width and Tortuosity Measurement

In this thesis, an automatic system was developed in order to analysis vascular system with regard to the special properties of the vessel such as diameter and tortuosity. The proposed system includes three main stages, vessel extraction, preprocessing, and vessel properties measurements. The hybrid feature vector and ensemble classifier was utilized for extracting the network of blood vessels. In the following step, a preprocessing algorithm is introduced for preparing the correspond network for further analysis. In the last stage, the two important algorithms based on the edges and centerline of fragmented vessels were utilized for measuring and analyzing the diameter and tortuosity of blood vessels.

In the diameter measurement step, one of the most popular method introduced by Nguyen et al. (2013) was utilized for measuring the diameter of retinal blood vessels. The corresponding algorithm for measuring the diameter of vessels is based on the edges and centerline of the fragmented vessels. The different analysis was proposed for extracting the meaningful information from the results of the width measurement algorithm. For instance, the histogram of the vessels width was plotted in order to determine the percentage of the thin vessels with respect to the entire network, since identifying the thin blood vessels and the percentage of them with regarding the entire vasculature system is an important task for prediction the diabetic retinopathy diseases. Moreover, the standard deviation of the each fragmented vessels with respect to the diameter of the each center points along the corresponding vessel is explored in the entire network for determining the presence of different diseases such

as diabetic retinopathy and plus disease. The vessel with a higher value of standard deviation than threshold value indicates the presence of several abnormalities. The important point that should be referred is that choosing the specific value of standard deviation as a threshold is an important task which can be determined by an expert. The other disadvantage of the corresponding analysis with regard to the standard deviation is that the corresponding parameter is very sensitive in such a way that any false detection of edges and center points along the fragmented vessels results in the wrong value of standard deviation. For accurate measuring the standard deviation of each fragmented vessel a local analysis can be introduced in such a way that in each fragmented vessel a set of standard deviations can be measured with respect to the specific connected components along vessel. And the mean value of the corresponding values can be considered as an accurate standard deviation.

An algorithm based on the chain code known as SCC was utilized for measuring the retinal blood vessels tortuosity. The different analysis was introduced with regard to the results of tortuosity measurements algorithm. For instance, in order to identify the vessels with a high value of tortuosity, the histogram of vessels tortuosity is plotted with respect to the entire vessel network. Moreover, a single value of tortuosity is defined by measuring the mean value of tortuosity in the network. The goal of measuring the corresponding mean value is that the tortuosity value of the entire vessel network in different images can be easily compared using a single value correspond analysis is that the specifying the constant value of tortuosity as a threshold value for separating different images as normal or abnormal images is very difficult task that can be determined by an expert.

The important point that should be noticed is that the proposed method for measuring the width and tortuosity of blood vessel in different images depends on the several conditions. The most important and necessary condition for comparing the two images with regard to the diameter and tortuosity values is that the images must be captured in the same scale. However, there is no suitable available database.

5.3 Feature Work

The automatic software tool for retinal blood vessel analysis can be developed as a future work. The goal of this work is to create a computer assisted diagnostic system by gathering or combining different kind of measurements. These measurements includes artery and vein classification, identifying artery-vein-cross sections, measures the diameter of arteries and veins separately in order to achieve A/V ratio. Moreover, a general tortuosity value can be introduced with regard to the diameter and length of vessels by specifying different weights.

REFERENCES

Abramoff, M.D., Garvin, M.K., & Sonka, M. (2010). Retinal imaging and image analysis. *IEEE Reviews in Biomedical Engineering, 3*(1), 169-207.

Azzopardi, G., Strisciuglio, N., Vento, M., & Petkov, N. (2015). Trainable COSFIRE filters for vessel delineation with application to retinal images. *Journal of Medical Image Analysis, 19*(1), 46-57.

Al-Rawi, M., Qutaishat, M., & Arrar, M. (2007). An improved matched filter for blood vessel detection of digital retinal images. *Computers in Biology and Medicine, 37*(2), 262-267.

Al-Diri, B., Hunter, A., & Steel, D. (2009). An active contour model for segmenting and measuring retinal vessels. *IEEE Transactions on Medical Imaging, 28*(9), 1488-1497.

Bribiesca, E. (2013). A measure of tortuosity based on chain coding. *Pattern Recognition, 46*, 716-724.

Breiman, L. (2001). Random forests. *Machine Learning, 45*(1), 5–32.

Brinchmann-Hansen, O., & Heier, H. (1986). The apparent and true width of the blood column in retinal vessels. *Acta Ophthalmologica, 64*(179), 29-32.

Browing, D.J. (2010). *Diabetic retinopathy: Diabetic macular edema.* New York: Springer.

Bullitt, E., Gerig, G., Pizer, S.M., Lin, W., & Aylward, S.R. (2003). Measuring tortuosity of the intracerebral vasculature from MRA images. *IEEE Transactions on Medical Imageing, 22*(9), 1163-1171.

Chiang, A., Witkin, A.J., Regillo, C.D., & Ho, A.C. (2011). *Age-related macular degeneration diagnosis and treatment: Fundus imaging of age related macular degeneration*. New York: Springer.

Chutatape, O., Zheng, L., & Krishnan, S. (1998). Retinal blood vessel detection and tracking by matched Gaussian and Kalman filters. *Proceedings of the 20th Annual International Conference of the IEEE Engineering in Medicine and Biology Society, 6*(1), 3144-3149.

Chaudhuri, S., Chatterjee, S., Katz,N., Nelson, M., & Goldbaum, M. (1989). Detection of blood vessels in retinal images using two-dimensional matched filters. *IEEE Transactions on Medical Imaging, 8*(3), 263-269.

Cheng, E., Du, L., Wu, Y., Zhu, Y. J., Megalooikonomou, V., & Ling, H. (2014). Discriminative vessel segmentation in retinal images by fusing context-aware hybrid features. *Machine Vision and Applications, 25*(1), 1779-1792.

Fritzsche, K., Can, A., Shen, H., Tsai, C., Turner, J., Tanenbuam, H.L., et al. (2003). *Angiography and plaque imaging: Automated model based segmentation, tracing and analysis of retinal vasculature from digital fundus images.* Oca Raton, FL: CRC, 225-298.

Fraz, M.M., Barman, S., Remagnino, P., Hoppe, A., Basit, A., Uyyanonvara, B., et al. (2012). An approach to localize the retinal blood vessels using bit planes and center line detection. *Computer Methods and Programs in Biomedicine, 108*(2), 600-616.

Frangi, A.F., Niessen, W. J., Vincken, K. L., & Viergever, M. A. (1998). *Medical image computing and computer-assisted interventation—MICCAI'98: Multi scale vessel enhancement filtering,* USA: Springer, 130–137.

Fraz, M.M., Remagnino, P., Hoppe, A., Uyyanonvara, B., Rudnicka, A. R. Owen, C. G., et al. (2012). An ensemble classification-based approach applied to retinal blood vessel segmentation. *IEEE Transactions on Biomedical Engineering, 59*(9), 2538-2548.

Foracchia, M. (2001). Extraction and quantitative description of vessel features in hypertensive retinopathy fundus images. *Book Abstracts 2nd International Workshop on Computer Assisted Fundus Image Analysis.*

Fraz, M.M. (2013). *Retinal image segmentation and quantification of vessel width in non-standard retinal datasets.* Ph.D. Thesis, Kingston University of London, United Kingdom.

Grisan, E., & Ruggeri, A. (2003). A divide et impera strategy for automatic classification of retinal vessels into arteries and veins. *Proceedings of the 25th Annual International Conference of the IEEE Engineering in Medicine and Biology Society, 1*(1), 890-893.

Gao, X., Bharath, A., Stanton, A., Hughes, A., Chapman, N., & Thom, S. (2001). A method of vessel tracking for vessel diameter measurement on retinal images. *Proceedings of International Conference of the IEEE* in *Image Processing, 2*(1), 881-884.

Grisan, E., Pesce, A., Giani, A., Foracchia, M., & Ruggeri, A. (2004). A new tracking system for the robust extraction of retinal vessel structure. *Proceedings of the 26th Annual International Conference of the IEEE Engineering in Medicine and Biology Society, 1*(1), 1620-1623.

Goh, K.G. Wynne, H., Lee, M.L., & Wang, H. (2001). Adris: An automatic diabetic retinal image screening system. *Medical Data Mining Knowledge Discovery*, 181-210.

Gang, L., Chutatape, O., & Krishnan, S. (2002). Detection and measurement of retinal vessels, in fundus images using amplitude modified second-order Gaussian filter. *IEEE Transactions on Biomedical Engineering, 49*(2), 168-172.

Gregson, P.H., Shen, Z., Scott, R.C., & Kozousek, V. (1995). Automated grading of venous beading. *Computers and Biomedical Research, 28*(4), 291-304.

Grisan, E., Foracchia, M., & Ruggeri, A. (2008). A novel method for the automatic grading of retinal vessel tortuosity. *IEEE Transactions on Medical Imaging, 27*(3), 310-319.

Heneghan, C., Flynn, J., O'Keefe, M., & Cahill, M. (2002). Characterization of changes in blood vessels width and tortuosity in retinopathy of prematurity using image analysis. *Medical Image Analysis, 6*(1), 407-429.

Haddouche, A., Adel, M., Rasigni, M., Conrath, J., & Bourennane, S. (2010). Detection of the foveal avascular zone on retinal angiograms using Markov random fields. *Digital Signal Processing, 20*(1), 149-154.

Hoover, A., & Goldbaum, M. (2003). Locating the optic nerve in a retinal image using the fuzzy convergence of the blood vessels. *IEEE Transactions on Medical Imaging, 22*(8), 951-958.

Huiqi, L., & Chutatape, O. (2004). Automated feature extraction in color retinal images by a model based approach. *IEEE Transactions on Biomedical Engineering, 51*(2), 246-254.

Hoover, A., Kouznetsova, V., & Goldbaum, M. (2000). Locating blood vessels in retinal images by piece wise threshold probing of a matched filter response. *IEEE Transactions on Medical Imaging, 19*(3), 203-210.

Hart, W.E., Goldbaum, M., Côté, B., Kube, P., & Nelson, M.R. (1997). Automated measurement of retinal vascular tortuosity. *Proceedings of the AMIA Annual Fall Symposium,* 459-463.

Hart, W.E., Goldbaum, M., Côté, B., & Kube, P. (1999). Measurement and classification of retinal vascular tortuosity. *International Journal of Medical Informatics, 53*(3), 239-252.

Hall, M.A., & Smith, L.A. (1998). Practical feature subset selection for machine learning. *Proceedings of the 21th Australasian Computer Science Conference ACSC'98 in Springer*, 181-191.

Iqbal, M.I., Gubbal, A.M., & Khan, A. (2006). *Automatic diagnosis of diabetic retinopathy using fundus images*. Master Thesis, Blenkinge Institute of Technology, Sweden.

Jiang, X., & Mojon, D. (2003). Adaptive local thresholding by verification-based multi- threshold probing with application to vessel detection in retinal images. *IEEE Transactions on Pattern Analysis and Machine Intelligence, 25*(1), 131-137.

Klein, B., Klein, R., Hall, E., Lee, K., & Jensen, K. (2004). The compatibility of estimates of retroilluminated lens opacities as judged from film-based and digital imaging. *American Journal of Ophthalmology, 138*(1), 668-670.

Kanski, J.J., & Bowling, B. (2011). *Clinical ophthalmology: A systematic approach.* (7th ed.). United Kingdom: Elsevier Health Sciences.

Lowell, J., Hunter, A., Steel, D., Basu, A., Ryder, R., & Kennedy, R.L. (2004). Measurement of retinal vessel widths from fundus images based on 2-D modeling. *IEEE Transactions on Medical Imaging, 23*(10), 1196-1204.

Liu, I., & Sun, Y., (1993). Recursive tracking of vascular networks in angiograms based on the detection deletion scheme. *IEEE Transactions on Medical Imaging, 12*(2), 334-341.

Laud, K., & Shabto, U. (2010). *Principle of diabetic mellitus: Diabetic retinopathy*. (2th ed.). New York: Springer.

Larsen, H.W. (1976). The ocular fundus: A color atlas. *Munksgaard, Copenhagen, Denmark.*

Li, W., Bhalerao, A., & Wilson, R. (2007). Analysis of retinal vasculature using a multi resolution hermite model. *IEEE Transactions on Medical Imaging, 26*(2), 137-152.

Lupascu, C.A., Tegolo, D., & Trucco, E. (2010). FABC: Retinal vessel segmentation using Ada Boost. *IEEE Transactions on Information Technology in Biomedicine, 14*(5), 1267-1274.

Lotmar, W., Freiburghaus, A., & Bracher, D. (1979). Measurement of vessel tortuosity on fundus photographs. *Albrecht von Graefe Archiv fur klinische und experimentelle Ophthalmologie, 211*(1), 49-57.

Lam, B.S., Gao, Y., & Liew, A.C. (2010). General retinal vessel segmentation using regularization-based multi concavity modeling. *IEEE Transactions on Medical Imaging, 29*(7), 1369-1381.

Lam, L., Lee, S.W., & Suen, C.Y. (1992). Thinning methodologies-a comprehensive Survey. *IEEE Transactions on Pattern Analysis and Machine Intelligence, 14*(9), 869-885.

Michaelson, I.C., & Benezra, D. (1980). *Textbook of the fundus of the eye*. (3th ed.). United Kingdom: Churchill Livingstone, Edinburgh.

Mendonca, A. M., & Campilho, A. (2006). Segmentation of retinal blood vessels by combining the detection of center lines and morphological reconstruction. *IEEE Transactions on Medical Imaging, 25*(9), 1200-1213.

Martinez-Pérez, M.E., Hughes, A.D., Thom, S.A., Bharath, A.A., & Parker, K.H. (2007). Segmentation of blood vessels from red-free and fluorescein retinal images. *Medical Image Analysis*, *11*(1), 47-61.

Miri, M.S., & Mahloojifar, A. (2011). Retinal image analysis using curvelet transformand multistructure elements morphology by reconstruction. *IEEE Transactions on Biomedical Engineering, 58*(5), 1183–1192.

Marin, D., Aquino, A., Gegúndez-Arias, M., & Bravo, J. (2011). A new supervised method for blood vessel segmentation in retinal images by using gray-level and moment invariants-based features. *IEEE Transactions on Medical Imaging 30*(1), 146-158.

Niemeijer, M., Staal, J., van Ginneken, B., Loog, M., M. & Abramoff, M.D. (2004). Comparative study of retinal vessel segmentation methods on a new publicly available database. *SPIE Medical Imaging, 5370*(1), 648-656.

Narasimha-Iyer, H., Beach, J. M., Khoobehi, B., & Roysam, B. (2007). Automatic identification of retinal arteries and veins from dual-wavelength images using structural and functional features. *IEEE Transactions on Biomedical Engineering, 54*(8), 1427-1435.

Nguyen, U.T.V., Bhuiyan, A., Park, L.A.F., & Ramamohanarao, K. (2013). An effective retinal blood vessel segmentation using multi-scale line detection. *Pattern Recognition, 46*(3), 703-715.

Oloumi, F. (2011). *Analysis of the vascular architecture in fundus images of the retina*. Master Thesis, the University of Calgary, Alberta.

Patton, N., Aslam, T.M., MacGillivray, T., Deary, I.J., Dhillon, B., Eikelboom, R.H., et al. (2006). Retinal image analysis: Concepts, applications and potential. *Progress in Retinal and Eye Research, 25*(1), 99-127.

Pinz, A., Bernogger, S., Datlinger, P., & Kruger, A. (1998). Mapping the human retina. *IEEE Transactions on Medical Imaging, 17*(4), 606-619.

Pizer, S., Amburn, E., Austin, J., Cromartie, R., Geselowitz, A., Greer, T., et al. (1987). Adaptative histogram equalization and its varations. *Computer Vision, Graphices, and Image Processing, 39*(3), 355–368.

Ricci, E., & Perfetti, R. (2007). Retinal blood vessel segmentation using line operators and support vector classification. *IEEE Transactions on Medical Image, 26*(10), 1357-1365.

Solouma, N.H., Youssef A.B.M., Badr, Y.A., & Kadah Y.M. (2002). A new real-time retinal tracking system for image-guided laser treatment. *IEEE Transactions on Biomedical Engineering, 49*(9), 1059-1067.

Sum, K.W., & Cheung, P.Y.S. (2008). Vessel extraction under non-uniform illumination: A level set approach. *IEEE Transactions on Biomedical Engineering, 55*(1), 358-360.

Sinthanayothin, C., Boyce, J., Cook, H., & Williamson, T. (1999). Automated localisation of the optic disc, fovea, and retinal blood vessels from digital colour fundus images. British Journal of Ophthalmology, *83*(8), 902-910.

Staal, J., Abràmoff, M.D., Niemeijer, M., Viergever, M.A., & van-Ginneken, B. (2004). Ridge- based vessel segmentation in color images of the retina. *IEEE Transactions on Medical Imaging, 23*(4), 501-509.

Strouthidis, N.G., & Garway, D.F. (2009). *Glaucoma: Detecting glaucoma progression by imaging.* Berlin: Springer.

Soares, J.V.B., Leandro, J.J.G., Cesar-Jr, R.M., Je- linek, H.F., & Cree, M.J. (2006). Retinal vessel segmentation using the 2-D Gabor wavelet and supervised classification. *IEEE Transactions on Medical Imaging, 25*(9), 1214-1222.

Teng, T., Lefley, M., & Claremont, D. (2002). Progress towards automated diabetic ocular screening: A review of image analysis and intelligent systems for diabetic retinopathy. *Medical and Biological Engineering and Computing, 40*(1), 2-13.

Wong, T.Y., Klein, R., Sharrett, A.R., Duncan, B.B., Couper, D.J., Tielsch, J.M., et al. (2002). Retinal arteriolar narrowing and risk of coronary heart disease in men and women. *The Journal of the American Medical Association, 287*(9), 1153-1159.

Wilson, C.M., Cocker, K.D., Moseley, M.J., Paterson, C., Clay, S.T., Schulenburg, W.E., et al. (2008). Computerized analysis of retinal vessel width and tortuosity in premature infants. *Investigative Ophthalmology and Visual Science, 49*(1), 3577–3585.

Wolff Eugene. (1948). *The anatomy of the eye and orbit*. (3th ed.). H. K. Lewis & Co. Ltd., London.

You, X., Peng, Q., Yuan, Y., Cheung, Y.M., & Lei, J. (2011). Segmentation of retinal blood vessels using the radial projection and semi-supervised approach. *Pattern Recognition, 44*(10), 2314–2324.

Zhang, B., Zhang, L., Zhang, L., & Karray, F. (2010). Retinal vessel extraction by matched filter with first-order derivative of Gaussian. *Computers in Biology and Medicine, 40*(4), 438-445.

Zana, J., & Klein, C. (2001). Segmentation of vessel-like patterns using mathematical morphology and curvature evaluation. *IEEE Transactions on Image Processing, 10*(7), 1010-1019.

Zhu, X., Rangayyan, R.M., & Ells, A.L. (2011). Digital image processing for ophthalmology: Detection of the optic nerve head. *Synthesis Lectures on Biomedical Engineering, 6*(1), 1-106.

APPENDICES

LIST OF ABBRIVIATIONS

DR ..... Diabetic retinopathy
PDR ..... Proliferative diabetic retinopathy
DME ..... Diabetic macular edema
AMD ..... Age related macular degeneration
CNV ..... Choroidal neovascularization
ROP ..... Retinopathy of prematurity
DRIVE ..... Digital retinal image for vessel extraction
STARE ..... Structured analysis of the retina
FOV ..... Field of view
TP ..... True positive
TN ..... True negative
FP ..... False positive
FN ..... False negative
Acc ..... Accuracy
SN ..... Sensitivity
SP ..... Specificity
PPV ..... Positive predictive value
ROC ..... Receiver operating characteristic
AUC ..... Area under the curve
TPR ..... True positive rate
FPR ..... False positive rate
SVM ..... Support vector machine
KNN ..... K-nearest neighbor
MLP ..... Multilayer perceptron
RS ..... Random subspace
RF ..... Random forest
WLD ..... Weber local description
LBP ..... Local binary pattern

SCC.....Slope chain code
ROI.....Region of interest
DoG.....Difference of Gaussians